



**HAL**  
open science

## Moisture amplification of the high-altitude deglacial warming

Etienne Legrain, P. Blard, Masa Kageyama, Julien Charreau, Guillaume Leduc, Stella Bourdin, David V. Bekaert

► **To cite this version:**

Etienne Legrain, P. Blard, Masa Kageyama, Julien Charreau, Guillaume Leduc, et al.. Moisture amplification of the high-altitude deglacial warming. *Quaternary Science Reviews*, 2023, 318, pp.108303. 10.1016/j.quascirev.2023.108303 . hal-04301517

**HAL Id: hal-04301517**

**<https://hal.science/hal-04301517>**

Submitted on 23 Nov 2023

**HAL** is a multi-disciplinary open access archive for the deposit and dissemination of scientific research documents, whether they are published or not. The documents may come from teaching and research institutions in France or abroad, or from public or private research centers.

L'archive ouverte pluridisciplinaire **HAL**, est destinée au dépôt et à la diffusion de documents scientifiques de niveau recherche, publiés ou non, émanant des établissements d'enseignement et de recherche français ou étrangers, des laboratoires publics ou privés.

# 1        **Moisture amplification of the high-altitude deglacial warming**

2        Etienne Legrain<sup>1\*</sup>, Pierre-Henri Blard<sup>2,3\*</sup>, Masa Kageyama<sup>4</sup>, Julien Charreau<sup>2</sup>, Guillaume Leduc<sup>5</sup>, Stella  
3        Bourdin<sup>4</sup>, David V. Bekaert<sup>2</sup>

4        1 - Université Grenoble Alpes, CNRS, IRD, Grenoble INP, IGE, Grenoble, France

5        2 - CRPG, CNRS, Université de Lorraine, 54000 Nancy, France

6        3 - Laboratoire de glaciologie, DGES-IGEOS, Université Libre de Bruxelles, 1050 Brussels, Belgium

7        4 - LSCE/IPSL, UMR CEA-CNRS-UVSQ 8212, Université de Paris-Saclay, Gif-sur-Yvette, France

8        5 - Aix-Marseille Université, CNRS, IRD, INRAE, Coll. France, CEREGE, 13545 Aix-en-Provence,  
9        France

10       \*Corresponding authors: [etienne.legrain@univ-grenoble-alpes.fr](mailto:etienne.legrain@univ-grenoble-alpes.fr), [pierre-henri.blard@cnrs.fr](mailto:pierre-henri.blard@cnrs.fr)

11

## 12 **Abstract**

13 In response to anthropogenic warming, glaciers are shrinking almost everywhere, endangering  
14 water accessibility in areas located downstream. Glacier fluctuations are at first order controlled by local  
15 precipitation and temperature, but large uncertainties persist on the potential role of local moisture in  
16 amplifying or dampening temperature changes at high-elevation. Here, we combine glacier extents and  
17 Sea Surface Temperature (SST) during the Last Glacial Maximum (LGM) to quantify altitudinal thermal  
18 gradients (lapse rate) from 40°N to 40°S along the American Cordillera. We also constrain modern lapse  
19 rates based on present day temperature and SST database to explore how the lapse rate has changed  
20 since the LGM along this North South transect. Based on proxy-based quantitative paleo-precipitation  
21 estimations above 2000 m, we investigate how these lapse rate changes compare with moisture  
22 modifications around the Cordillera and discuss the mechanisms that potentially controlled lapse rate  
23 changes during the post-LGM deglacial warming.

24 We find that lapse rate changes are linearly related to changes in precipitation and derive a  
25 quantitative relationship between these two parameters. To further explore the processes involved in  
26 controlling lapse rate variations, we use the IPSL global climate model outputs, for the LGM and pre-  
27 industrial states in this region. The IPSL model also yields a shallower modern lapse rate in the wetter  
28 tropical region, confirming the observed correlation between precipitation changes and lapse rate  
29 variations. The IPSL model also supports a close coupling of continental relative moisture and mean  
30 annual precipitation in the studied area, indicating that moisture is involved in the precipitation – lapse  
31 rate relationship. Our results suggest that future warming may be enhanced in high altitude regions  
32 where precipitation is expected to increase. Using our most reliable relationship linking precipitation  
33 and lapse rate changes, we conclude that, assuming a 1°C warming at sea level, a mean annual  
34 precipitation increases of 500 mm.a<sup>-1</sup> could lead to a warming amplification of  $4.1 \pm 0.8^\circ\text{C}$  at 4000 m  
35 asl (mean elevation of modern glaciers). In this case, a 2°C warming at sea level would yield  $> 6^\circ\text{C}$   
36 degrees warming at 4000 m asl. This study therefore confirms that special attention should be given to  
37 the climate projections of glacier melting in tropical and mid latitude regions.

38

## 39 **Main text**

### 40 **1 - Introduction**

41 Global warming massively disrupts the cryosphere at low and mid-latitude, as alpine glaciers  
42 shrinking is now accelerating worldwide (Hugonnet et al., 2021; Thompson et al., 2011). Over the last  
43 two decades, melting of mountain glaciers (excluding ice cap) has contributed to  $21 \pm 3\%$  of the global  
44 sea level rise, i.e. more than Greenland and Antarctica considered separately (Hugonnet et al., 2021;  
45 Slater et al., 2020). In mountainous regions where precipitation is highly seasonal, alpine glaciers

46 represent the main water supply during the dry season (Kaser et al., 2010; Pritchard, 2019; Rabatel et  
47 al., 2013). It is therefore crucial to identify factors that modulate glacier melting in order to better  
48 understand and anticipate their stability, for the decades to come (Kraaijenbrink et al., 2017; Zekollari  
49 et al., 2019).

50 The annual mass balance of a glacier is primarily controlled by mean local temperature and  
51 precipitation (Condom et al., 2007; Ohmura, 1992). Globally, the temperature increase associated with  
52 anthropogenic fossil fuel combustion recently surpassed  $+1^{\circ}\text{C}$ , at an average warming rate of  $+0.18$   
53  $^{\circ}\text{C}/\text{decade}$  (Intergovernmental Panel on Climate Change (IPCC), 2022). This warming rate is not  
54 spatially homogenous: it is notably amplified over the continent, reaching on average  $1.4^{\circ}\text{C}$  in the  $40^{\circ}\text{S}$ -  
55  $40^{\circ}\text{N}$  zone at low elevation (Seltzer et al., 2023a). At high elevation, in mountainous areas,  
56 anthropogenic warming has reached up to  $+0.7^{\circ}\text{C}/\text{decade}$  (Intergovernmental Panel on Climate Change  
57 (IPCC), 2022). However, high elevation warming rates are very variable from one region to another,  
58 ranging between  $+0.1$  and  $+0.7^{\circ}\text{C}/\text{decade}$  above  $2000\text{ m}$  (Pepin, 2015). Many potential causes for high-  
59 altitude temperature amplification have been proposed, including surface albedo feedbacks, latent heat  
60 release, moisture-enhanced radiative changes, and aerosol feedbacks (Pepin, 2015). These mechanisms  
61 may at least partly explain the contrasting regional patterns of high-altitude warming, but the relative  
62 contributions of each of these forcing remain unknown.

63 Several studies have hypothesized that warming at high altitude should be greater than observed  
64 at sea level because warmer conditions at the regional scale will increase the atmospheric moisture  
65 content and yield a shallower lapse rate. The modern global annual average free atmospheric lapse rate  
66 (LR) is  $-6.5^{\circ}\text{C}\cdot\text{km}^{-1}$ , but it locally varies between the moist adiabat value around  $4\text{--}6^{\circ}\text{C}/\text{km}$  and the dry  
67 adiabat value of  $-9.8^{\circ}\text{C}\cdot\text{km}^{-1}$  (Stone and Carlson, 1979). The temporal and spatial LR variations remains  
68 poorly known. Accurate and precise reconstructions of paleo LR under different global and regional  
69 paleo-climate conditions are useful to quantify and understand how the atmospheric moisture content  
70 may affect LR variations at the regional scale (Blard et al., 2007a; Loomis et al., 2017; Tripathi et al.,  
71 2014a).

72 Recent compilations of oceanic and continental paleothermometers proposed that the global  
73 post-Last Glacial Maximum (LGM) warming was between  $4\text{--}6^{\circ}\text{C}$ , with large regional disparities (Annan  
74 et al., 2022; Seltzer et al., 2021; Tierney et al., 2020). Even if the exact amplitude of the post LGM  
75 warming could still be refined in future studies, the LGM climate is an ideal benchmark for studying the  
76 sensitivity of global temperatures to the net radiative forcing, and the specific responses of certain  
77 regions, partly driven by the polar amplification (Smith et al., 2019), the terrestrial amplification (Seltzer  
78 et al., 2023) or by the altitudinal dependent warming (Pepin et al., 2015). LGM temperature  
79 reconstructions at high elevations have yielded contrasting results: some tropical and mid latitude  
80 regions display an amplified post-LGM warming at high elevation (steeper LR during the LGM) (Blard  
81 et al., 2007a; Kuhlemann et al., 2008; Loomis et al., 2017), while others suggest no dependence of the  
82 post-LGM warming on elevation (i.e., no LR change since the LGM) (Tripathi et al., 2014a). These

83 studies provide local reconstructions in different regions of the globe, with contrasting hydrological  
84 regimes. Thus, they may not be globally representative, hampering our ability to anticipate potentially  
85 upcoming LR changes under future climatic conditions.

86 In this study, we aim to fill this gap by investigating the main physical parameters and  
87 mechanisms controlling LR changes. For that, we compare reconstructed precipitation and LR data  
88 between the LGM and present. We focus our study on the American Cordillera, along a near-continuous,  
89 8000 km-long latitudinal transect ranging from 40°N to 40°S. From Alaska to Patagonia, the American  
90 Cordillera is the sole mountain range that continuously covers both Hemispheres over a large latitudinal  
91 range (70°N – 50°S, **Fig. 1**), with a mean altitude of 4000 m and summits above 6000 m asl. The  
92 American Cordillera thus provides a unique collection of glaciers, encompassing both the tropics and  
93 mid-latitude regions. The Cordillera also have sub-regions with very contrasting precipitation regimes,  
94 which is ideal to test the potential impact of moisture variations on LR changes. It is also located near  
95 the Eastern Pacific Ocean, where records of SSTs permit constraining low altitude LGM temperatures.  
96 Local continental precipitation proxies (e.g., lake levels, speleothems, and pollen records) are also  
97 available in the vicinity of LGM paleoglaciers. Here, based on glacier paleo-extents, we reconstruct  
98 LGM equilibrium lines of the American cordillera glaciers and convert them into 0°C isotherm altitudes  
99 using independent estimates of paleoprecipitation, following the approach of Condom et al., (2007) and  
100 Legrain et al., (2022). We then combine these paleo-isotherm estimates with alkenone-based paleo SST  
101 data to compute LGM LR estimates along the latitudinal transect. These LR estimates are then  
102 compared with present-day LR values (computed with a comparable methodology) to identify where  
103 and how LR have changed during the last deglaciation. The mechanisms causing the observed spatial  
104 and temporal LR variability are then investigated using the IPSL global climate model outputs, for LGM  
105 and pre-industrial states.

106

## 107 **2 – Materials and Methods**

108 To reconstruct LR variations between the LGM and today, our approach includes four main steps  
109 (summarized on the synoptic flow diagram presented in **Supplementary Fig. 1**), which involve both  
110 already published and newly computed data :

- 111 1. Identifying sites with LGM glacial extents, well-dated by cosmogenic  $^{10}\text{Be}$ ,  $^{36}\text{Cl}$  or  
112 radiocarbon (section 2.1.). The locations of the paleoclimatic data used in this study are  
113 presented in **Supplementary Figs. 3-4**.
- 114 2. Compiling /determining modern (section 2.2.) and LGM (section 2.3.) SST, 0°C isotherm  
115 and precipitation for each site considered. For the LGM, this step notably requires  
116 reconstructing LGM ELAs using the Accumulation-Area Ratio (AAR) method and

- 117 converting these into LGM 0°C isotherms using empirical relationship linking ELA,  
118 temperature, and paleoprecipitation data (Fox and Bloom, 1994; Legrain et al., 2022).
- 119 3. Converting SST data into equivalent continental sea-level temperatures at the sites where  
120 glacial landforms are studied using an empirical transfer function (section 2.4.).
  - 121 4. Computing modern and LGM lapse rates (with LGM LR defined as the slope between SST  
122 – taken at -125 m below present-day sea level – and the glacier-derived isotherm 0°C  
123 elevation) to derive  $\Delta LR$  values by subtracting the LGM LR from the modern LR (section  
124 2.5.).

125 We then proceed to a model-data comparison (section 2.6.) using outputs of the IPSLCM5A2 model  
126 (Sepulchre et al., 2020) to investigate the underlying mechanism(s) controlling LR temporal and spatial  
127 variations.

## 128 **2.1 - Studied LGM glacial landforms and their ages constraints**

129 This study is based on the compilation of well-dated LGM landform extents dated by *in situ*  
130 cosmogenic nuclides (27/31 sites) and radiocarbon (4/31 sites) (Supplementary Tabs. 1 and 2). The  
131 inclusion criteria for these LGM glacial extents is to consider that every glacial morphology dated  
132 between 26-18 ka belongs to the LGM. This 26-18 ka range represents the broad duration of the global  
133 LGM (Clark et al., 2009). Considering this whole time window has the advantage to account for the  
134 inter-site age variability produced by the slight diachronism of the so-called “local” LGMs identified  
135 along the American Cordillera (Palacios et al., 2020).

136 <sup>10</sup>Be cosmogenic data used here comprise all the published LGM ages stored within the online  
137 ICE-D database <http://alpine.ice-d.org/>. All these <sup>10</sup>Be exposure ages are updated and homogenized  
138 using the KNSTD07 standardization (Nishiizumi et al., 2007), and are recomputed with the online  
139 calculator Cosmic Ray Exposure Program (CREp) <https://crep.otelo.univ-lorraine.fr/#/> (Martin et al.,  
140 2017) using the regional production rate of the Andes (Martin et al., 2015), as well as the world wide  
141 mean value, for comparison (Supplementary Tab. 2) (Martin et al., 2017). For comparison, we also  
142 compute these <sup>10</sup>Be ages using two different scaling schemes: *Lal stone time corrected* (Lal, 1991) and  
143 *Lifton-Sato-Dunai* (Lifton et al., 2014) (Supplementary Tab. 2). In all cases, we use the ERA40  
144 atmosphere model and the atmospheric <sup>10</sup>Be based Virtual Dipolar Moment (VDM) (Muscheler et al.,  
145 2005) to account for time variations of the production rate. Our comparison shows that the choice of the  
146 scaling and production rates does not affect the final ages beyond uncertainties (Supplementary Tab. 2).  
147 We retain the ages computed with the *Lal stone time variable* scaling with the regional Andes production  
148 rate (Martin et al., 2015). In the few cases where no regional production rate is available (southern  
149 Andes), we use the <sup>10</sup>Be ages computed with the worldwide mean production rate (Supplementary Tab.  
150 2). <sup>36</sup>Cl ages of landforms (n=7) are considered without any additional processing (Supplementary Tab.

151 1) as there is no consensus on  $^{36}\text{Cl}$  elemental production rates (Marrero et al., 2016; Schimmelpfennig  
152 et al., 2009).

153 When no direct cosmogenic surface exposure age of a given glacial morphology is available (as  
154 is the case for 4 sites in Ecuador and Colombia; Supplementary Tab. 1), the age of the morphology is  
155 determined by  $^{14}\text{C}$  dating on paleosoils bracketing the glacier moraines.

## 156 **2.2 - Modern temperatures and precipitation at the studied sites**

### 157 *2.2.1. Modern Sea Surface Temperatures*

158 We use the modern SST data from the Extended Reconstructed Sea Surface Temperature  
159 version 4 (ERSST\_V4) (Huang et al., 2015; Smith and Reynolds, 2003), available at  
160 <https://www.esrl.noaa.gov/psd/>. This database is based on SST values extended from the  
161 Comprehensive Ocean–Atmosphere Data Set (COADS) database. Modern SSTs correspond to the mean  
162 annual value from the climatic period 1989-2018 (Supplementary Tab. 3). Data are compiled for each  
163 0.5 latitudinal degree from 40°N to 40°S along the American Pacific coast and the Venezuelan and  
164 Colombian Caribbean coasts. We use the Pacific Ocean SSTs, except for the Santa Maria Colombian  
165 site and the Venezuelan sites, that are closest to the Caribbean Sea (Supplementary Tab. 3). At these  
166 two locations, we compute a mean SST between the Pacific and the Caribbean zone. It is noteworthy  
167 that SST values from the Pacific Ocean and the Caribbean Sea are similar ( $\Delta\text{SST} \leq 1^\circ\text{C}$ ) at these latitudes  
168 (12-9°N). Thus, the potential bias induced by combining the Pacific Ocean and Caribbean Sea data is  
169 not considered as a significant source of uncertainty in our study.

### 170 *2.2.2. Modern 0°C isotherms*

171 Modern 0°C isotherms are directly compiled from literature data (Supplementary Tab. 5), except  
172 for the Sierra Nevada and San Bernardino sites, for which no previous estimate of the 0°C isotherm is  
173 available. For the sites from Sierra Nevada and San Bernardino, we estimate the 0°C isotherm using  
174 normal PRISM reanalysis data (1980-2011). We extract data for 118 sites of high-altitude glaciers and  
175 perform a regression of elevation as a function of mean annual temperature (**Supplementary Fig. 6**),  
176 yielding an averaged value of 0°C isotherm for the whole range of  $3578 \pm 22$  m ( $2\sigma$ , standard deviation).  
177 Computed and compiled modern 0°C isotherms range from 3452 to 5100 m with an average of 4530  
178  $\pm 587$  m ( $1\sigma$  standard deviation). We estimate an approximate uncertainty of 50m for modern 0°C  
179 isotherms directly compiled from literature.

### 180 *2.2.3. Modern precipitation*

181 The values of modern precipitation at the LGM precipitation sites are PRISM product, that is  
182 compiled from high-resolution radar measurements (Western Regional Climate Center,  
183 <https://wrcc.dri.edu/>), from global modelling of precipitation (Climate Change Knowledge Portal,

184 <https://climateknowledgeportal.worldbank.org>), and from climatic station measurements  
185 (Supplementary Tab. 6).

186

## 187 **2.3 – LGM temperatures and precipitation at the studied sites**

### 188 *2.3.1. LGM Sea Surface Temperatures*

189 To reconstruct SSTs during LGM, we use alkenone data from 16 marine cores located along the  
190 American cordillera at a restricted distance (<1000 km) from the coastline (**Fig. 1; Supplementary Fig.**  
191 **2**). We use a single SST proxy approach to avoid potential biases due to interproxy disparities (Bova et  
192 al., 2021; Leduc et al., 2017, 2010). Moreover, alkenone is the only SST proxy available from marine  
193 cores along the whole American Cordillera (**Fig. 1**) and comparison of SST proxies suggest that  
194 alkenones provide accurate SST estimates in the Tropics (Lea et al., 2014). The LGM alkenone-derived  
195 SSTs are averaged from 26 to 18 ka (Supplementary Tab. 8). To estimate LGM SSTs corresponding to  
196 the sites studied for glacial landforms, we first consider a simple linear extrapolation between the  
197 reconstructed SSTs for the two nearest LGM SST cores.

198 Importantly, this simple approach may suffer biases due to the heterogeneous spatial distribution of  
199 marine cores. To circumvent this issue and smooth local discrepancies, we consider time variations of  
200 the SST and how they may relate to latitude. Because the Holocene variability of temperature is low,  
201 we assume in this calculation that the modern SSTs are equivalent to Holocene average SSTs derived  
202 from alkenone data. For the Holocene, we average the alkenone-derived SST for the time period 11.7 to  
203 0 ka. We consider the Holocene as a whole because global temperature changes during this period were  
204 marginal ( $1\sigma$  standard deviation  $<1^\circ\text{C}$ ) and the averages should therefore represent robust and  
205 representative SST values. Then we consider the LGM SST as the mean of the 26-18 ka period. The  
206  $\Delta\text{SST}$  (Holocene-LGM) are then calculated as the difference between the mean Holocene SST and the  
207 mean LGM SST (Supplementary Tab. 8).

208 As expected, the minimal  $\Delta\text{SST}$  values are found around the equator and increase exponentially  
209 towards higher latitudes, suggesting that alkenone data provide LGM SST estimates that are precise  
210 enough to capture the polar temperature amplification (**Fig. 2**). At  $\sim 34^\circ\text{N}$ , we observe a cluster of LGM  
211 SST anomalies that are much lower than surrounding estimates from other marine sites. These LGM  
212 SST anomalies of  $\sim -1^\circ\text{C}$  compared to modern SST are caused by an early warming in the area, more  
213 than 10 ka before the end of the LGM (Herbert et al., 2001). This early SST warming was likely caused  
214 by the collapse of the California Current during glacial maximum, in response to a local climate change  
215 occurring on land (Herbert et al., 2001). Using the local LGM SST defined for  $\sim 25$  ka from these 3 cores  
216 would yield LGM anomalies of about  $-4^\circ\text{C}$ , a value in good agreement with other SST estimates at those  
217 latitudes (Herbert et al., 2001, **Fig. 2**). As this LGM SST anomaly is very localized and is not

218 representative of the large-scale latitudinal trend, we remove these three sites from our LGM SST  
219 database (labelled in red in **Fig. 2**). As the  $\Delta$ SST are driven at first order by latitude, we can use it to  
220 compute the LGM SST at each latitude location from the modern SST. From these data, we then define  
221 a relationship between  $\Delta$ SST at any given latitude and the latitude (**Fig. 2**):

$$222 \quad \Delta\text{SST}(\text{latitude}) = A \times \exp(|\text{Latitude}| \times B) \quad (\text{S1})$$

223 where Latitude is expressed in decimal degrees (DD) and A and B are empirical parameters specific to  
224 the eastern Pacific SST latitudinal gradient. This LGM SST at any given latitude, especially at studied  
225 sites for glacier paleoextents, can be calculated by subtracting the latitude-specific  $\Delta$ SST from the  
226 modern SST at the same latitude.

227

### 228 *2.3.2. LGM 0°C isotherms*

229 ELA, 0°C isotherm and mean annual precipitation are linked with robust empirical relationships  
230 (Condom et al., 2007; Fox and Bloom, 1994; Legrain et al., 2022). Knowing this relationship and LGM  
231 precipitation (see section 3.3.3 below, Supplementary Tabs. 5 and 6) allows using LGM ELAs and LGM  
232 precipitation to compute LGM 0°C Isotherm elevations. To estimate paleo ELAs from paleo glacial  
233 extents we use the Accumulation Ablation Ratio (AAR) (Meier and Post, 1962) method, that is a robust  
234 and easy-to-use technique (Benn and Lehmkuhl, 2000). The AAR defines the ELA as the elevation at  
235 which the ratio between (i) the glacier area above this ELA and (ii) the total surface of the glacier, equals  
236 the AAR (Meier and Post, 1962) (i.e., the ratio of the accumulation area to the area of glacier). Thus,  
237 the LGM ELA can be computed if both the total surface of the LGM glacier and the AAR are known.

238 The LGM glacial extent and total surface of each studied glacier are determined by glacial  
239 morphology analysis and identification of lateral and frontal moraines mapped using high-resolution  
240 Landsat imagery (**Supplementary Fig. 7**). Then, we assume that the AAR remained constant through  
241 time and estimate paleo-ELA based on the modern AAR. Since AAR may vary spatially, we use the  
242 most accurate AAR estimates available (from the World Glacier Monitoring Service (WGMS) mass  
243 balance measurements) to calibrate regional AAR values (**Supplementary Fig. 8**). Following Martin et  
244 al. (2020), we compile interannual AAR and annual mass balances to estimate the AAR value  
245 (**Supplementary Fig. 8**) of each glacier, at equilibrium with the climate state. Data from modern glaciers  
246 available in WGMS permitted to calibrate AARs in the following five regions: the Sierra Nevada (n=1  
247 glacier), Mexico (n=1), the Central Andes (n=1), the Bolivian and the Peruvian Andes (n=2)  
248 (Supplementary Tab. 7). In the case of Venezuela and Central America, for which modern data are  
249 absent from the WGMS database, we use AAR regional values directly compiled from the literature  
250 (Stansell et al. (2007) (Venezuela) and Lachniet and Vazquez-Selem (2005) (Central America)  
251 (Supplementary Tab. 7).

252 Local LGM ELAs for each glacial valley are given in Supplementary Tab. 7. The final  
253 uncertainties associated with these ELAs are computed using the quadratic sum of the standard deviation  
254 associated with each regional AAR coefficient (ranging from 0.03 to 0.06) and a spatial uncertainty of  
255 50 m to account for the lack of precision of paleo glacier mapping.

256 For South and Central America (20°N – 36°S), we use the relationship calibrated by Fox and  
257 Bloom, (1994) to calculate the elevation of the LGM 0°C isotherm, Iso0<sub>LGM</sub> (m asl), as:

$$258 \quad \text{Iso0}_{\text{LGM}} = \text{ELA}_{\text{LGM}} - 3427 + (1148 \times \log_{10} P_{\text{LGM}}) \quad (\text{S2})$$

259 where  $P_{\text{LGM}}$  is the mean annual precipitation ( $\text{mm.a}^{-1}$ ) and  $\text{ELA}_{\text{LGM}}$  is the Equilibrium Line Altitude (m  
260 asl), both during the LGM. This equation is established for the latitudinal range of 5-17°S but was proven  
261 to yield robust and accurate results between 10°N and 50°S (Condom et al., 2007). In Central America  
262 (20°N – 10°N), climatic conditions are fairly similar to the calibration area (Tropical Andes), implying  
263 that this equation is likely to also provide robust results for this region.

264 For the Sierra Nevada and San Bernardino Mountains (40°N – 34°N), we use the relationship  
265 established by Legrain et al. (2022) who used data from Northern America glaciers to define a regional  
266 version of the Fox and Bloom, (1994) equation:

$$267 \quad \text{Iso0}_{\text{LGM}} = \text{ELA}_{\text{LGM}} - 5150 + (1640 \times \log_{10} P_{\text{LGM}}) \quad (\text{S3})$$

268 Total uncertainties on LGM 0°C Isotherms are computed by propagating uncertainties on LGM  
269 precipitation, LGM ELA, as well as the calibration relationship.

270

### 271 *2.3.3. LGM precipitation*

272 A few LGM precipitation databases exist (Bartlein et al., 2011; Cleator et al., 2019) and were  
273 used in climate-model comparison exercises (e.g. Kageyama et al., 2021). Unfortunately, only very few  
274 quantitative LGM precipitation estimates are included in these databases for western America. A few  
275 isotopic records based on speleothems (Lachniet et al., 2013) and leaf wax (Bhattacharya et al., 2018)  
276 are available, but as the isotopic composition of rainfall records mixed source signals, precipitation  
277 temperatures, and extents of Rayleigh-type distillation, comparing isotopic results from the LGM and  
278 Holocene is not straightforward. In particular, the deglacial warming and continental ice sheet melting  
279 invariably obscure precipitation signals and eventually compromise quantitative precipitation rate  
280 estimates. For this reason, we ignore rainfall estimates based on stable isotopes. Instead, we derive LGM  
281 precipitation from other proxies (pollen assemblage, paleolake shoreline, packrat midden)  
282 (Supplementary Tab. 6) that provide relative precipitation change between the LGM and modern  
283 conditions. In practice, we compute LGM precipitation by correcting modern precipitation from these  
284 changes derived from these proxies (Supplementary Tab. 6, **Fig. 3**). When uncertainties are not provided

285 in the original publication, we arbitrarily attribute a relative uncertainty of 20% for LGM precipitation  
286 estimates.

287

## 288 **2.4 – Continental effect: translation of SST into continental-equivalent temperature**

289 We restrict our compilation to the American Cordillera in order to minimize the potential bias  
290 introduced by the effect of continentality between SST and 2m air temperatures above continents.  
291 Despite the relative proximity ( $\leq 500\text{km}$ ) between the glaciated sites in the Andes Cordillera and the  
292 Pacific Ocean (or the Caribbean Sea), a correction must be applied to convert modern and LGM coastal  
293 SST into equivalent continental sea-level temperatures. This correction accounts for the fact that  
294 continents have a different radiative budget and climatic inertia compared to the ocean (Seltzer et al.,  
295 2023).

296 In order to compute this continental-ocean correction for the present day, we compile weather  
297 station data at variable altitudes along the American cordillera, and defined 9 regions  
298 (**Supplementary Fig. 5-6**) whereby the LR appears to be distinct from those of the adjacent areas  
299 (spatial LR variability  $> 1^\circ\text{C}/\text{km}$ ). Each region is also characterized by a specific climate. For instance,  
300 the distinction between San Bernardino Mountains and Sierra Nevada corresponds to an abrupt change  
301 in precipitation rates (Pandey et al., 1999) associated with an orographic depression ( $<1000\text{ m asl}$ )  
302 between these two regions. For Mexico, we separate an Eastern and a Western Transmexican region,  
303 since available climatic data show strong differences in the atmosphere thermal structures of these two  
304 regions (spatial LR variability  $\geq 1.5^\circ\text{C}\cdot\text{km}^{-1}$ ). These differences are probably due to the influences of  
305 Caribbean Sea and Pacific Ocean on the corresponding coastal sites. In this case, the boundary between  
306 the two regions at a given latitude is defined as the equidistant point between the two coasts. The Central  
307 America region conforms to the specific climate of Central America, with a geographical setting  
308 characterized by high moisture transport across the Central America isthmus (Leduc et al., 2007).  
309 Equatorial Andes are divided into two distinct regions: the Northern and the Southern Equatorial Andes,  
310 representing the Colombian Venezuelan Andes (Caribbean Sea influence and discontinuous Andes) and  
311 the Peruvian Bolivian Andes (Pacific coast and high-altitude plateau), respectively. The Northern  
312 Central Andes correspond to the climatic region of the Chilean Dry Andes, characterized by a near  
313 absence of glaciers due to extremely dry conditions (Ammann et al., 2001). The Southern Central Andes  
314 correspond to the glaciated region South of the North Central Andes.

315 For each region, we compile mean annual temperature data from weather stations (wrrc.dri.edu;  
316 explorador.cr2.cl; <http://berkeleyearth.lbl.gov>). Combining the elevation and temperature of these  
317 station, we obtain the temperature of the theoretical 0 m asl altitude within the mountain range, for each  
318 of the 9 sub-climatic regions (**Supplementary Fig. 9**). This theoretical temperature is referred to as the  
319 CNET (Continental Null Elevation Temperature). Then, we compare this value with the modern SST of

320 the East Pacific at the same latitude and expressed the Correction Factor of Continental Effect (CFCE)  
321 as:

$$322 \quad \text{CFCE (i)} = \text{CNET(i)} - \text{SST(i)} \quad (\text{S4})$$

323 where (i) corresponds to the index of a given climatic region. The mean CFCE value is  $+4.3 \pm 5.2$  °C,  
324 ranging from  $+14.8$ °C (Bolivian and Peruvian Andes) down to  $-2.3$ °C (Central America)  
325 (Supplementary Tab. 4). Then, we compute the modern  $\text{SST}_{\text{corr}}$  for each of the 31 studied sites:

$$326 \quad \text{SST}_{\text{corr}}(\text{modern})(i) = \text{SST}_{\text{Modern}} - \text{CFCE}(i) \quad (\text{S5})$$

327 where CFCE is given in °C and varies for each calibrated region. Modern SSTs data corrected for the  
328 continental effect using the regional computed CFCE value are reported in Supplementary Tab. 3.

329 To compute the continental-ocean correction for the LGM, we use the same approach as for  
330 modern data but we apply an additional correction to account for continental amplification. Recently,  
331 it has been shown that during a major climatic change, the temperature change over the continent is  
332 about 37% larger than that of the ocean (Seltzer et al., 2023a). To compute the SST during the LGM  
333 period we thus account for the terrestrial amplification of the post-deglacial warming. Hence, the  
334  $\text{SST}_{\text{corr}}$  (LGM) is:

$$335 \quad \text{SST}_{\text{corr}}(\text{LGM}) = \text{SST}_{\text{Modern}} + \text{CFCE} - 1.37 \times (\Delta\text{SST}) \quad (\text{S6})$$

336 with  $\Delta\text{SST}_{\text{LGM}}$  defined by equation (S1).

337  $\text{SST}_{\text{corr}}$  (LGM) values are reported in Supplementary Tab. 3.

## 338 **2.5 - Lapses rate and $\Delta\text{LR}$ computations**

339 We compute both modern and LGM LR using a linear interpolation between a high-altitude  
340 temperature (glacier data) and a zero-altitude temperature (continental temperature reconstruction  
341 derived from coastal SSTs), following:

$$342 \quad \text{LR}(t) = \frac{-\text{SST}_{\text{corr}}(t)}{\text{Iso0}(t) - Z(\text{SST}_{\text{corr}}(t))} \quad (\text{S7})$$

343 Where (t) refers to either the LGM or modern time,  $\text{Iso0}(t)$  is the 0°C isotherm elevation in m asl. at  
344 the considered time t,  $\text{SST}_{\text{corr}}(t)$  and  $Z(\text{SST}_{\text{corr}}(t))$  are the SST corrected from the CFCE (°C) and the  
345 altitude of the  $\text{SST}_{\text{corr}}(t)$  compared to the modern value, respectively, both also at the considered time  
346 t. In practice, we use  $Z(\text{SST})$  values of 0 and -125 m for the modern and LGM sea level (Dutton et al.,  
347 2015; Fleming et al., 1998), respectively. The last step of our procedure is to compute the difference  
348 between the two LR in order to get the  $\Delta\text{LR}$  (in °C.km<sup>-1</sup>) for the 31 glacial sites along the American  
349 cordillera (Supplementary Tab. 9).

350

## 351 **2.6 IPSLCM5A2 climate model**

352 The model results used in this study are based on the IPSLCM5A2 model (Sepulchre et al.,  
353 2020). The pre-industrial simulation is described in the same reference. The LGM simulations follows  
354 the PMIP4 protocol (Kageyama et al., 2017) and is further described in the first overview of PMIP4  
355 LGM simulations (Kageyama et al., 2021). The main changes in boundary conditions to obtain this  
356 LGM simulation are those due to the LGM ice sheets: the altitude, land ice extent and coastlines are set  
357 up following the PMIP3 ice sheet reconstruction (Abe-Ouchi et al., 2015). Greenhouse gases and  
358 insolation parameters are set up to their LGM values (Kageyama et al., 2017). The Pre-industrial  
359 simulation has been run for 2800 years up to equilibrium (Sepulchre et al., 2020). The LGM simulation  
360 has been run for 1200 years, starting from pre-industrial conditions. The final 100 years of the pre-  
361 industrial and LGM experiments are used to define the averages used in the present work. We examine  
362 the 3D (longitude, latitude, altitude) annual mean temperatures and relative humidity simulated by the  
363 model for both periods, over the Americas and adjacent oceans, as well as the annual mean precipitation.

364 We compute the free atmospheric lapse rate for each grid point as the slope of the regression of  
365 the vertically dependent temperature vs altitude of the grid point, computed by using the mean  
366 geopotential height. Grid points with altitude below 6000m are retained.

367

## 368 **3 – Results**

### 369 **3.1 – Low altitude vs high altitude temperature changes**

370 **Fig. 4a** displays the post-LGM warming on the continent at low elevation and at high elevation  
371 (computed from the 0° isotherm shift), respectively, from -40° to 40° latitude. This shows that low  
372 elevation T changes are comparable or slightly higher than those at high elevation, from 40°S to 10°S  
373 of latitude and beyond 35°N of latitude, with warming ranging from 1 to 6°C. A contrasting pattern is  
374 visible in the inner Tropics, between, 8°S to 20°N, where high elevation post LGM warming are  
375 significantly larger (8 to 14°C) than those observed at low elevation (1 to 6°C). Consequently, the lapse  
376 rate changes consecutive to the deglacial warming are much larger in this Inner Tropic region than those  
377 observed at higher latitudes and are locally driven by the large temperature changes that occurred at high  
378 elevation (**Fig. 4a**).

379

### 380 **3.2 - Comparing LGM and modern lapse rates**

381 Reconstructed LR values for LGM and modern time stand between  $-9.5 \pm 0.8$  and  $-3.8$   
382  $\pm 0.3^\circ\text{C.km}^{-1}$  (average LR of  $-6.7 \pm 1.6^\circ\text{C.km}^{-1}$ ;  $1\sigma$ ) and between  $-7.3$  and  $-5.2^\circ\text{C.km}^{-1}$  (average LR of -

383  $6.1 \pm 0.7 \text{ }^\circ\text{C.km}^{-1}$ ;  $1\sigma$ ), respectively (Table S9; **Fig. 4b, Fig. 5**). The interquartile range of LGM LR is  
384 markedly larger than the one for modern LR (**Fig. 5**). The  $\Delta\text{LR}$  ranges from  $-1.5$  to  $+3.7 \text{ }^\circ\text{C.km}^{-1}$   
385 (Supplementary Tab. 9; **Fig. 4c**). Positive  $\Delta\text{LR}$  values, indicative of shallower modern lapse rates  
386 relative to LGM, are observed in the Colombian Andes (Inner Northern Tropics), whereas slightly  
387 negative  $\Delta\text{LRs}$  are recorded in Northern and Southern Mid-latitudes. Shallower modern lapse rates  
388 indicate amplified post LGM warming at high elevation, compared to sea level. In the search for a spatial  
389 relationship between  $\Delta\text{LR}$  and latitude along the American Cordillera, we identify three distinct regions  
390 (**Fig. 4c**): **(i)** between  $\sim 40$  and  $20^\circ\text{N}$  (Sierra Nevada and San Bernardino mountains), where the modern  
391 LR is slightly steeper than the LGM LR (mean  $\Delta\text{LR}$  of  $-1.1 \pm 0.4^\circ\text{C.km}^{-1}$ ), **(ii)** between  $20^\circ\text{N}$  and  $9^\circ\text{S}$ ,  
392 where the modern LR is shallower than the LGM LR (mean  $\Delta\text{LR}$  of  $1.9 \pm 0.9^\circ\text{C.km}^{-1}$ ), and **(iii)** between  
393  $14^\circ\text{S}$  and  $35^\circ\text{S}$ , where the modern LR is similar to the LGM LR ( $\Delta\text{LR}$  average of  $-0.2 \pm 0.5^\circ\text{C.km}^{-1}$ ). In  
394 summary, a high-altitude amplification of post LGM warming is observed at low latitudes ( $20^\circ\text{N}$  to  
395  $9^\circ\text{S}$ ), in the central and the northern South American Cordillera (**Fig. 4**).

396 The  $\Delta\text{LR}$  simulated by IPSLCM5A2 (**Fig. 6g**) is positive over the tropical Americas, the  
397 maximum value being reached over northern South America. On the other hand, negative values are  
398 simulated over mid-latitude North America. Even if the simulated  $\Delta\text{LR}$  are much smaller than the  
399 reconstructed values, these model results suggest that changes in lapse rates are indeed spatially  
400 heterogeneous.

401

## 402 **4 – Discussions**

### 403 **4.1 Robustness of the reconstructed $\Delta\text{LR}$**

404 The robustness of our  $\Delta\text{LR}$  could be questioned because our approach includes several  
405 computation steps with inherent uncertainties, assumptions and corrections. However, several  
406 independent arguments and observations support our results and suggest our approach is robust.

407 First, as a sensitivity test, we also calculated the modern LR directly from weather station data  
408 (**Supplementary Fig. 5**). The average difference between these modern LR estimates and our modern  
409 SST versus  $0^\circ\text{C}$  isotherm-based LR is only  $0.2^\circ\text{C.km}^{-1}$  on average, with a maximum of  $0.94 \text{ }^\circ\text{C.km}^{-1}$  for  
410 Costa Rican sites (**Supplementary Fig. 10**). Such a small difference between two independent methods  
411 appears negligible and within the uncertainty of our regional  $\Delta\text{LR}$  computation. It is much lower than  
412 the modern versus LGM variations of the LR we report here for the Tropics (**Fig. 4c**). In other words,  
413 using the alternative stations-based methodology would not significantly affect the  $\Delta\text{LR}$  changes  
414 computed in this study between  $20^\circ\text{N}$  –  $9^\circ\text{S}$  (**Supplementary Fig. 10**). Nonetheless, we prefer to keep  
415 the SST and  $0^\circ\text{C}$  isotherm-based approach to compute modern LR, for two main reasons: **(i)** we consider  
416 it preferable to use the same methodology for LGM and modern LR computation, and **(ii)** the weather

417 station-based methodology does not permit taking into account the local LR variability due to the large  
418 geographical range covered by a weather-station region.

419 Second, we show that the final  $\Delta LR$  values are not very sensitive to the choice of the method  
420 used to estimate the LGM SST at the studied site (either latitudinal correction to account for polar  
421 amplification or linear interpolation) (**Fig. 7**).

422 Third, we also performed a sensitivity analysis to assess how each parameter involved in the  
423 lapse rate reconstructions contribute to our  $\Delta LR$  estimates, and hence identify potential bias. For this,  
424 we computed the  $\Delta LR$  by iteratively suppressing each of the following corrections (**Fig. 7**): **(i)** the  
425 conversion of LGM glacier paleoELAs into  $0^{\circ}\text{C}$  isotherms using independent precipitation estimates,  
426 **(ii)** the latitudinal interpolation of  $\Delta\text{SST}$ , and **(iii)** the conversion of modern and LGM SST into  
427 “equivalent” continental air temperatures with the CFCE. This sensitivity analysis indicates that the  
428 computed regional  $\Delta LR$  pattern remains similar, within uncertainty, when any of these three corrections  
429 is not accounted for (**Fig. 7**). In the extreme scenario where the  $\Delta LR$  are computed without any of these  
430 three corrections being applied, positive  $\Delta LR$  values are still present beyond uncertainties in the  
431 equatorial region (**Fig. 7**). These sensitivity tests therefore demonstrate that the patterns of our  $\Delta LR$   
432 calculations are robust.

433

## 434 **4.2 The role of precipitation and humidity on LR changes**

### 435 4.2.1 Correlation between LR and precipitation variations

436 For both LGM and modern values, the steepest LR values ( $\leq -6.5^{\circ}\text{C}/\text{km}$ ) are only observed in  
437 the driest regions ( $P \leq 1000\text{mm}/\text{yr}$ ; **Fig. 5**). However, the relationship between absolute LR and annual  
438 precipitation remains unclear for both LGM and modern data (**Fig. 5**). The modern LR displays a lower  
439 spread than LGM LR and the relationship between LR and annual precipitation is less significant under  
440 the warmer climatic state of the modern compared to the colder LGM (**Fig. 5**). This different LR vs  
441 precipitation sensitivity suggests that boundary conditions matter, but the main drivers (average  
442 temperature, atmospheric  $\text{CO}_2$  concentrations, differences in atmospheric dynamics) still need further  
443 research to be identified. To better understand the mechanism(s) that control(s) spatial and temporal  
444 variations of LR, we evaluate the correlation between the computed  $\Delta LR$  and absolute precipitation  
445 changes ( $\Delta P = \text{modern precipitation} - \text{LGM precipitation}$ ) (**Fig. 8**). Precipitation proxies indicate that  
446 rainfall significantly increased between the LGM and the Holocene in the inner tropics ( $20^{\circ}\text{N} - 9^{\circ}\text{S}$ :  $\Delta P$   
447 range from 0 to  $+1400\text{ mm}\cdot\text{yr}^{-1}$ ), while it slightly decreased in the outer tropics and at mid-latitudes  
448 ( $10^{\circ}\text{S} - 35^{\circ}\text{S}$  and  $34^{\circ}\text{N} - 40^{\circ}\text{N}$ :  $\Delta P$  range from  $-15$  to  $-770\text{ mm}\cdot\text{yr}^{-1}$ ) (**Fig. 3**, Supplementary Tab. 6,  
449 **Supplementary Fig. 4**). Notably, pollen records and lake shoreline levels in Central America ( $20^{\circ}\text{N}$ -  
450  $9^{\circ}\text{S}$ ) indicate a significant precipitation increase from the LGM to the Holocene (Supplementary Tab.

451 6). Although these absolute precipitation estimates are based on different proxies with their own  
452 characteristics and potential biases, their good overall agreement depicts a consistent picture. In detail,  
453 differences between the absolute precipitation estimates for the inner and the outer tropics display a  
454 precipitation pattern which potentially reflects a global southward shift of the Intertropical Convergence  
455 Zone (ITCZ) during the LGM, from Central America to South America, and/or an intensification of the  
456 South American Summer Monsoon (SASM). This scenario is corroborated by several precipitation  
457 records in Southern America (Blard et al., 2011; Martin et al., 2020, 2018; McGee, 2020; Woods et al.,  
458 2020).

459 Importantly,  $\Delta LR$  values display a linear relationship with  $\Delta P$  ( $R^2 = 0.81$ ;  $p\text{-value} = 3.2 \times 10^{-11}$ )  
460 (Fig. 8). Shallower modern lapse rates are associated with higher modern precipitation rates compared  
461 to the LGM. Conversely, areas characterized by a limited precipitation change (or a slight aridification)  
462 in the modern period (still relative to the LGM) yield unchanged or only slightly negative  $\Delta LR$  values  
463 (Fig. 8).

#### 464 4.2.2 Robustness of the $\Delta LR$ versus $\Delta P$ relationship

465 The precipitation values are used in the computation of the LR values to convert ELAs into  $0^\circ\text{C}$   
466 isotherms. One could hence wonder whether the  $\Delta LR$  versus  $\Delta P$  relationship (Fig. 8) could result from  
467 a bias inherent to the method. To evaluate the influence of the precipitation-correction on the  $\Delta LR$  versus  
468  $\Delta P$  relationship, we compute a similar relationship but using  $\Delta LR$  values that have not been corrected  
469 for the effect of precipitation (Supplementary Fig. 12). This methodological choice represents an  
470 extreme case where ELAs are considered as equivalent to  $0^\circ\text{C}$  isotherm, which is not physically realistic  
471 (Condom et al., 2007; Legrain et al., 2022). However, this approach allows us to evaluate the extent to  
472 which the observed correlation between  $\Delta P$  and  $\Delta LR$  is due to the intervention of precipitation in the  
473 computation of  $\Delta LR$  values. Using this approach, we find that the correlation between  $\Delta P$  and  $\Delta LR$   
474 qualitatively stands qualitatively similar, (i.e., wetter sites still are associated with shallower lapse rate;  
475 Supplementary Fig. 12). This sensitivity test thus reinforces the robustness of the observed correlation  
476 between  $\Delta LR$  and  $\Delta P$ . Nevertheless, the slope of the linear relationship is modified, implying that  
477 quantitative estimates is affected by the choice of using the precipitation correction. Since the glacier  
478 ELAs are sensitive to absolute precipitation, we still consider the relationship using precipitation values  
479 in the LR computation as the most reliable approach (Fig. 8).

#### 480 4.2.3 Role of moisture in the $\Delta LR$ variations

481 Based on the relationship results, we propose that shallower lapse rates may result from a post-  
482 LGM increase of the atmospheric water content. When the atmospheric water content increases, the  
483 capacity of the atmosphere to transfer heat from low to high elevations by convective and radiative  
484 transfer is enhanced, yielding less steep lapse rates (Kattell et al., 2013; Stone and Carlson, 1979). Our

485 suggestion of a shallower modern LR relative to the LGM in the inner tropics (20°N – 9°S) corroborates  
486 local studies of Blard et al. (2007) and Loomis et al. (2017), who established less steep modern LR  
487 compared to LGM in Hawaii and Kenya, respectively. Alternatively, constant modern LR could have  
488 prevailed in some tropical regions (e.g., between 11°S and 30°S in this study, but also in Papua New  
489 Guinea, in the Western Pacific (Tripathi et al. 2014)). The main difference between these two regions is  
490 that the summits of New Guinea are subject to much higher precipitation than those of Hawaii and  
491 Mount Kenya ( $> 1000 \text{ mm.yr}^{-1}$  versus  $< 500 \text{ mm.yr}^{-1}$ ), and the local LR is hence close to the moist  
492 adiabatic typical range (around 4-6°C/km). While our results demonstrate a linear relationship between  
493  $\Delta\text{LR}$  and  $\Delta\text{P}$ , some of the noise in this correlation may be attributed to differences in the absolute  
494 climatic conditions of the glaciers. Specifically, mountainous areas experiencing very high precipitation  
495 levels ( $> 1000 \text{ mm/yr}$ ) are likely to be less influenced by changes in precipitation, making them less  
496 susceptible to recording a change in lapse rates. Moreover, paleo-precipitation records suggest that the  
497 modern climate conditions in Papua New Guinea are not significantly wetter than during the LGM  
498 (Denham and Haberle, 2008; Hope, 2009). The absence of precipitation changes between the LGM and  
499 the modern would explain the absence of significant variation of the LR computed in these areas.

500

#### 501 **4.3 What can we learn by comparing the paleoLR derived from paleoELA and those from the** 502 **IPSLCM5A2 climate model?**

503 The GCM modeled  $\Delta\text{LR}$  and  $\Delta\text{P}$  (Pre-industrial – LGM) map indicates a first order spatial  
504 agreement between the variations of these two metrics (**Fig. 9**). This is in line with the empirical  
505 correlation that we derive from our reconstruction based on high altitude continental proxies between  
506  $\Delta\text{LR}$  and  $\Delta\text{P}$  (**Fig. 8**). The GCM outputs also indicate a tight spatial correlation between  $\Delta\text{P}$  and the  
507 difference of relative humidity (noted  $\Delta\text{RH}$ ) (**Fig. 6**). This correlation between RH and precipitation  
508 changes is supported by the scatter plot (**Fig. 9b**) between these individual outputs retrieved from the  
509 GCM grid ( $R^2 = 0.65$ ). The observed correlation in the paleoclimate record between  $\Delta\text{P}$  and  $\Delta\text{LR}$  could  
510 hence reflect a close control of  $\Delta\text{RH}$  on  $\Delta\text{LR}$ . The fact that RH changes may be a major driver of LR  
511 changes is also confirmed by plotting these metrics extracted from the IPSLCM5A2 model output over  
512 and close to the American cordillera from 40°N to 40°S (Fig. 9c) ( $R^2 = 0.80$ ). The same plot realized  
513 between the modelled specific humidity and LR changes display a poorer correlation mainly due to the  
514 sites located north of 20°N where  $\Delta\text{LR}$  is negative (Supplementary Fig. 11;  $R^2 = 0.27$ ). These  
515 observations provide a strong support for the involvement of a moisture control on LR changes,  
516 increased relative humidity conditions implying shallower lapse rates (or drier conditions implying  
517 steeper lapse rates) (Fig. 9).

518

519           However, the agreement between the IPSL model outputs and our proxy-based reconstruction  
520 does not hold for regions that experienced a post LGM precipitation increase. In such cases, the model  
521 shows a saturation effect for  $\Delta LR$ , hence causing the overall  $\Delta LR$  response to be underestimated  
522 (**Fig. 8**). A comparison between present day precipitation rates and those modeled for PI conditions (**Fig.**  
523 **10**) shows that the IPSL model underestimates precipitation rates over the Amazonian basin, while  
524 overestimating precipitation rates in the Northern part of the Andes (Ecuador, Columbia). This could  
525 result from the low resolution of the topography, which causes a poor representation of the real altitude  
526 of the range, and, hence, an inaccurate representation of the orographic effect in this narrow part of the  
527 Cordillera (Fig. 10). There are also other long-recognized biases of the IPSL models, as discussed by  
528 (Sepulchre et al., 2020). This low resolution could cause post-LGM LR changes to be underestimated  
529 in Ecuador and Columbia, where GCM-modeled precipitation are overestimated at the location of  
530 glaciers ( $> 1500$  mm/a, compared to  $< 1000$  mm/a), implying that the modeled LRs are already close to  
531 a moist adiabatic value (around  $5^{\circ}\text{C}/\text{km}$ ), thus hampering any post-LGM LR change to be observed in  
532 the simulations. Finally, it is important to acknowledge that lapse rates measured along mountain slope  
533 may be decoupled from those observed in the adjacent free atmosphere (Pepin et al., 2015), especially  
534 in valleys. Since the IPSL model is run at  $\sim 300$  km resolution, it only has an incomplete description of  
535 the real topography, and therefore of the processes occurring within the mountain atmospheric boundary  
536 layer, well below the subgrid scale. This observation may partly explain some of the discrepancies  
537 between modelled LR and those derived from paleoELA reconstruction. Future studies could test this  
538 by performing high-resolution GCM simulations with a much higher resolution topography (i.e.,  $< 10$   
539 km grid cell).

540

#### 541 **4.4 Amplification of high-altitude temperature changes: implications for anthropogenic warming**

542           During the past decade, several studies have developed the concept of an elevation-dependant  
543 warming (Pepin, 2015; Wang et al., 2016, 2014). Recent observations have shown an amplification of  
544 the high-altitude warming, albeit this pattern seems to yield contrasting outcomes (Ohmura, 2012). A  
545 recent study based on noble gas reconstruction of continental temperature evidenced a larger post LGM  
546 warming over the continent relative to the oceans, even at elevations  $< 1000$  m (Seltzer et al., 2021). In  
547 order to test the robustness of the amplification of temperature changes that we obtain here for high  
548 elevations, we compute the post LGM warming values derived from paleo-glaciers and plotted them  
549 against the altitude of observation (**Fig. 11**). Our data correspond to high elevation (2500 m to 5000 m)  
550 post LGM warming ranging between  $6$  and  $14^{\circ}\text{C}$  in locations that were drier during the LGM, and  $0$  to  
551  $5^{\circ}\text{C}$  in locations that were wetter. For Brazil, noble gas paleotemperatures indicate a low altitude LGM  
552 cooling of  $5.4 \pm 0.6^{\circ}\text{C}$ , at an average elevation of  $600$  m (Seltzer et al., 2021; Stute et al., 1995). This  
553 value is at the low end of the range of post LGM warming computed in our study for higher altitudes.

554 This observation thus implies that the amplification of the post LGM warming is significant at high  
555 elevation, and exceeds the effect of pure continental amplification (Seltzer et al., 2023) (**Fig. 11**).

556 Many factors have been proposed to explain the peculiar trends of anthropogenic warming,  
557 including surface-based land use feedbacks (Zeng et al., 2021), as well as atmospheric radiative forcings  
558 and convective process (Keil et al., 2021; Mountain Research Initiative EDW Working Group, 2015).  
559 A recent study also mentioned the potential role of seasonality in modulating short term warming  
560 amplification at high-altitude (Qixiang et al., 2018).

561 Several studies had already identified correlations between lapse rate and humidity, both for  
562 present day (Comand and Soden, 2021; Li et al., 2015) and the LGM (Blard et al., 2007; Kuhlemann et  
563 al., 2008; Loomis et al., 2017). Previous reconstructions of LGM lapse rates yielded contrasting results  
564 from different regions (Blard et al., 2007; Kuhlemann et al., 2008; Loomis et al., 2017; Tripathi et al.,  
565 2014) but the scarcity of these LGM reconstructions and their lack of quantitative precipitation estimate  
566 did not permit to demonstrate a clear forcing mechanism. Our synthesis identifies for the first time a  
567 robust quantitative relationship between changes in lapse rate and changes in local precipitation (and  
568 probably relative humidity) during the post LGM warming. This finding permits to better understand  
569 and constrain the roles of precipitation and moisture on lapse rate modifications, temporal and spatial  
570 changes in moisture being able to drive variable interregional lapse rate changes at different elevations.  
571 Consequently, as evidenced by our dataset (**Fig. 4a**), the magnitude of the LGM cooling at high elevation  
572 has a high probability to have been spatially heterogenous, which represents a significant caveat to keep  
573 in mind when deriving a uniform and universal temperature change on land (Seltzer et al., 2023). Using  
574 the obtained relationship between precipitation rates and lapse rate changes (**Fig. 8**), we estimate the  
575 high-altitude amplification of the future warming, assuming mean annual precipitation changes  
576 modelled by 2100 projection scenarios. For instance, a precipitation increases of 500 mm.a-1 would lead  
577 to a  $-1.1^{\circ}\text{C.km}^{-1}$ . Hence, based on our most reliable  $\Delta\text{LR}-\Delta\text{P}$  relationship, we find that a sea level  $+1^{\circ}\text{C}$   
578 warming could induce an additional warming of  $4.1 \pm 0.8^{\circ}\text{C}$  at 4000 m asl ( $1\sigma$  standard deviation).  
579 Following this reasoning, we speculate that regions becoming increasingly wet as a result of climate  
580 change may coincide with regions where the low altitude anthropogenic warming will be amplified at  
581 high-altitude and potentially accelerate mountainous glaciers melting here despite the increase in  
582 precipitation. Reversely, in the regions that will become drier in the future, global warming could be  
583 attenuated at high elevation. Future modelling studies should help to quantify these  
584 amplification/attenuation mechanisms and better address future high-altitude climatic changes.

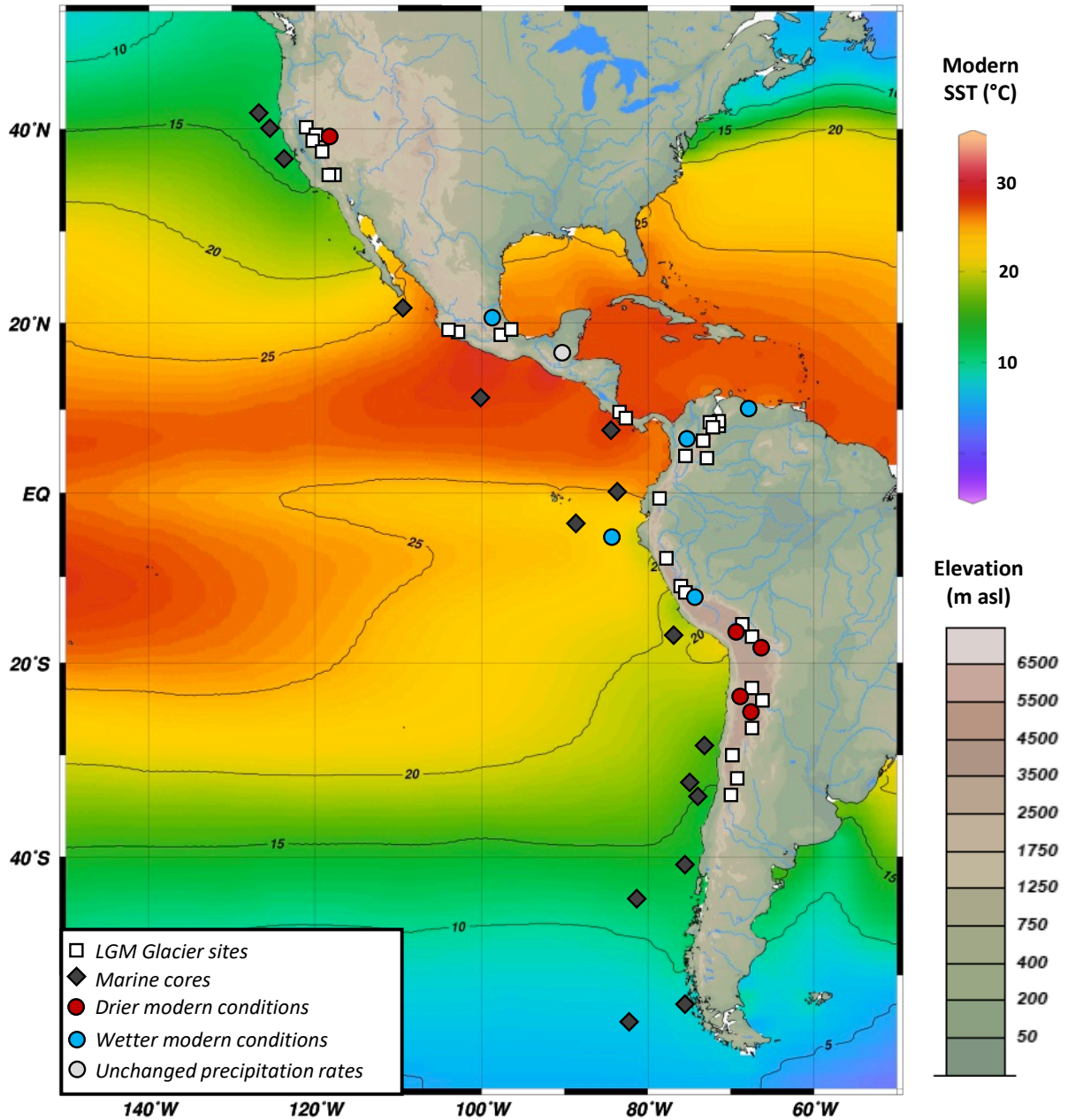
585

## 586 **5 – Conclusions**

587

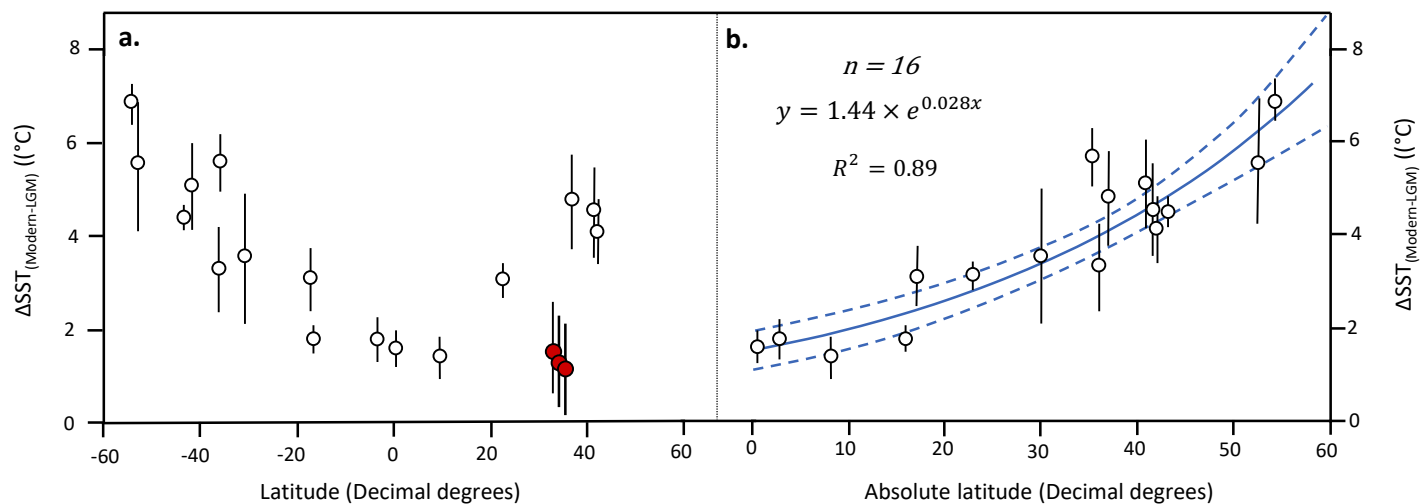
588 We summarize the main outcomes of our study in these four key findings:

- 589 • **Quantitative relationship between lapse rate and precipitation changes:** by using LGM  
590 0°isotherm from glacier paleo-equilibrium line, SST and paleoprecipitation proxies, we estab-  
591 lish a relationship linking post LGM changes in precipitation ( $\Delta P$ ) and changes in lapse rates  
592 ( $\Delta LR$ ).  
593
- 594 • **Amplified post-LGM warming in wetter areas:** the deglacial warming amplitude at high-  
595 altitude is correlated with changes in mean annual precipitation: in areas that have become wet-  
596 ter, the lapse rate has become shallower, and reversely. This mechanism is also encountered in  
597 the IPSL-GCM model outputs, although some discrepancies exist in regions that experienced  
598 the largest post LGM moisture increase.  
599
- 600 • **Spatial heterogeneities in post-LGM lapse rate variations:** by linking moisture and lapse rate  
601 changes, our study provides key insights to explain the heterogeneities in post-LGM lapse rate  
602 variations inferred from previous studies.  
603
- 604 • **Implications for anthropogenic-induced high-elevation warming:** our results suggest that  
605 the current high-altitude warming is underestimated in areas that will become wetter. Future  
606 modelled projections need to ensure that this moisture amplification mechanism is well captured  
607 by numerical models.  
608  
609



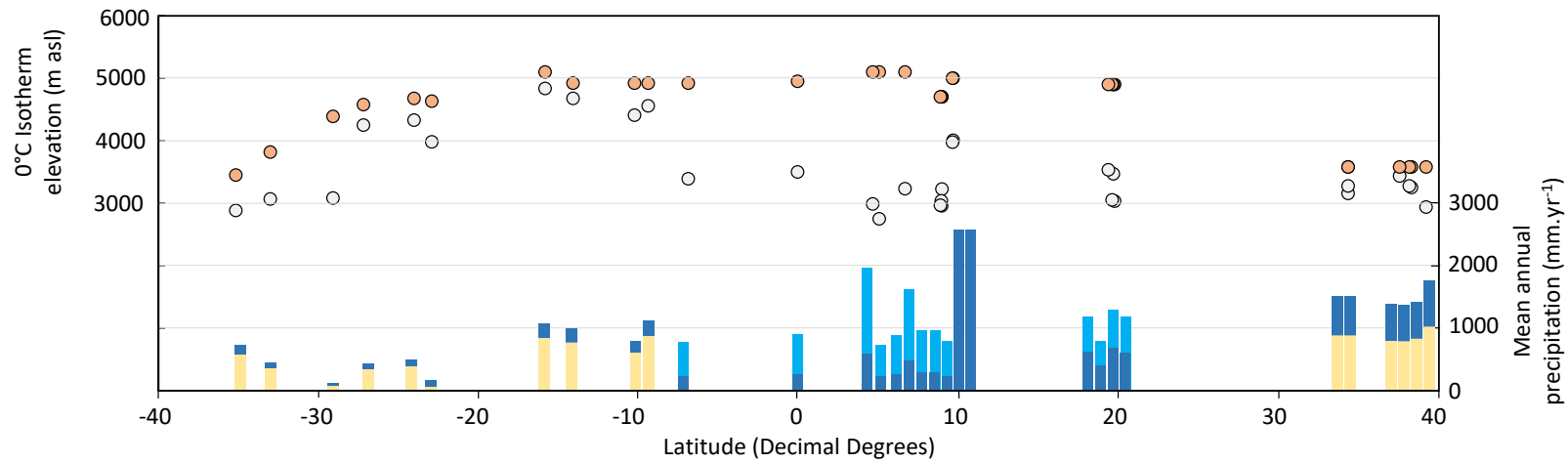
610

611 **Fig. 1:** Location of the studied sites. Grey diamonds identify marine core locations used for the SST calibration  
 612 (Fig.4). White squares are the 31  $\Delta$ LR computation sites. Dots are sites with LGM paleoprecipitation estimates.  
 613 Blue, red and grey dots respectively indicate sites where the modern period is wetter, drier, and unchanged than  
 614 LGM.



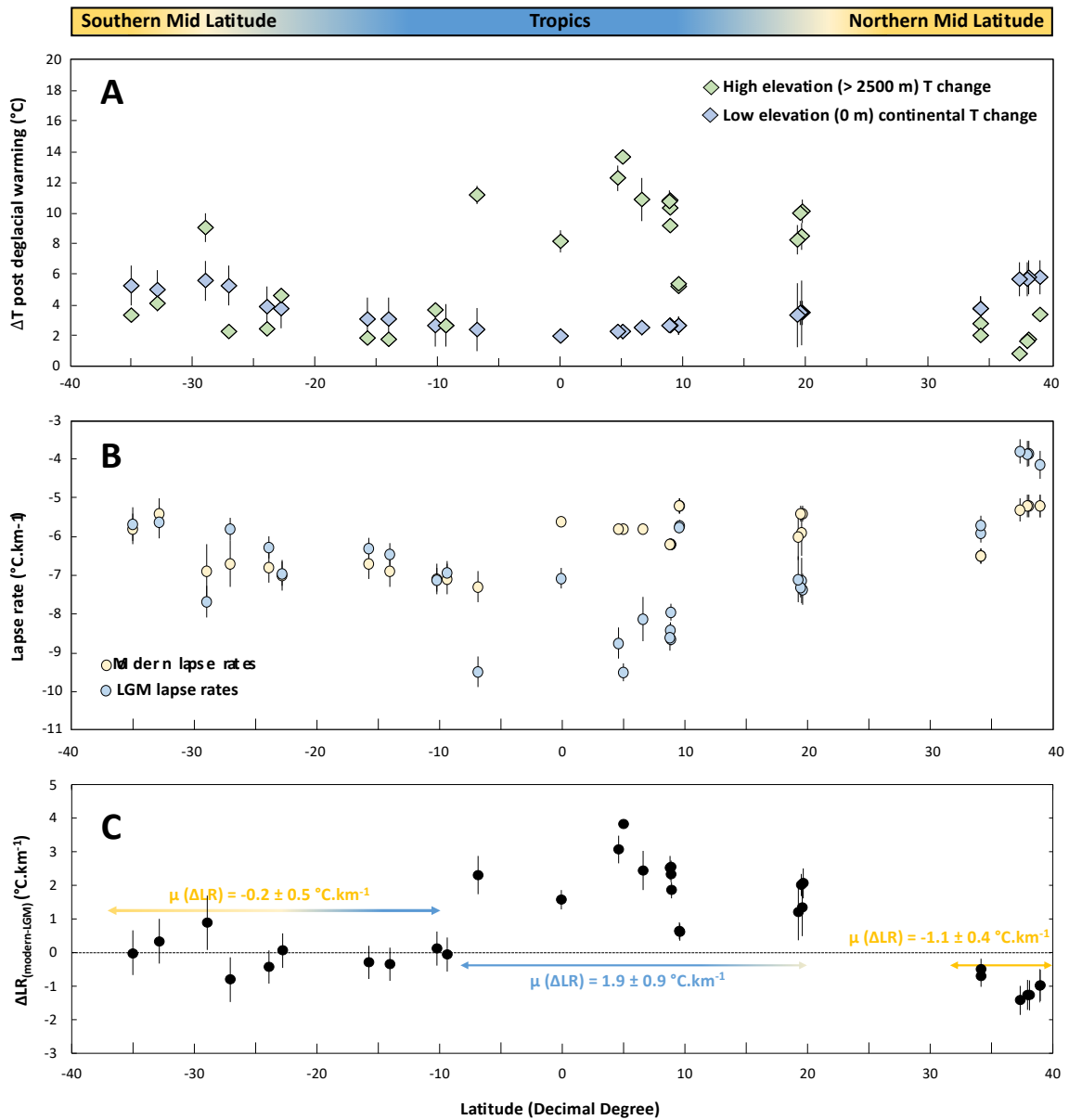
615

616 **Fig. 2:** Calibration of the  $\Delta SST_{(Modern-LGM)}$ . **a.** White and red dots are SST estimates from marine cores included in, and excluded from, the calibration, respectively (see Methods).  
 617 All SST estimates are based on alkenone reconstructions. The U-shaped relationship between the  $\Delta SST_{(Modern-LGM)}$  and latitude highlights the polar amplification. **b.**  $\Delta SST_{(Modern-LGM)}$   
 618 is plotted as a function of absolute latitude used to estimate the  $\Delta SST_{(Modern-LGM)}$  at each latitude (blue line). Dashed lines represent the  $1\sigma$  envelope ( $R^2 = 0.89$ ;  $MSWD =$   
 619  $1.3$ ;  $p$  value =  $2 \times 10^{-12}$ ).



620

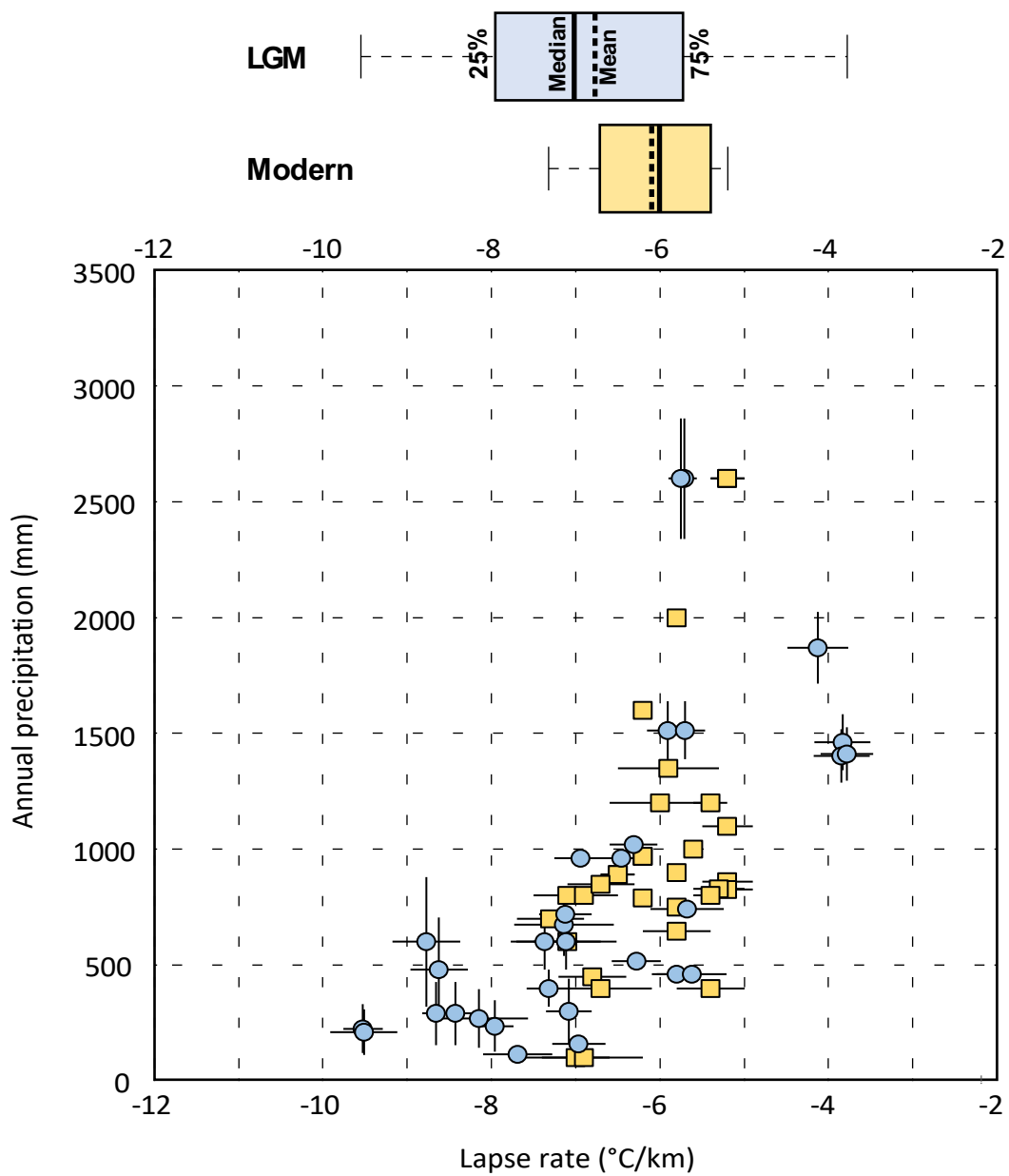
621 **Fig. 3:** Modern and LGM 0°C Isotherm elevation and associated precipitation changes. Red and grey circles are modern and LGM 0°C isotherm values, respectively. Dark  
 622 blue sticks are LGM precipitation at the Isotherm 0°C computation sites. Light blue and yellow sticks are modern precipitation when they are higher and lower than during  
 623 LGM, respectively.



624

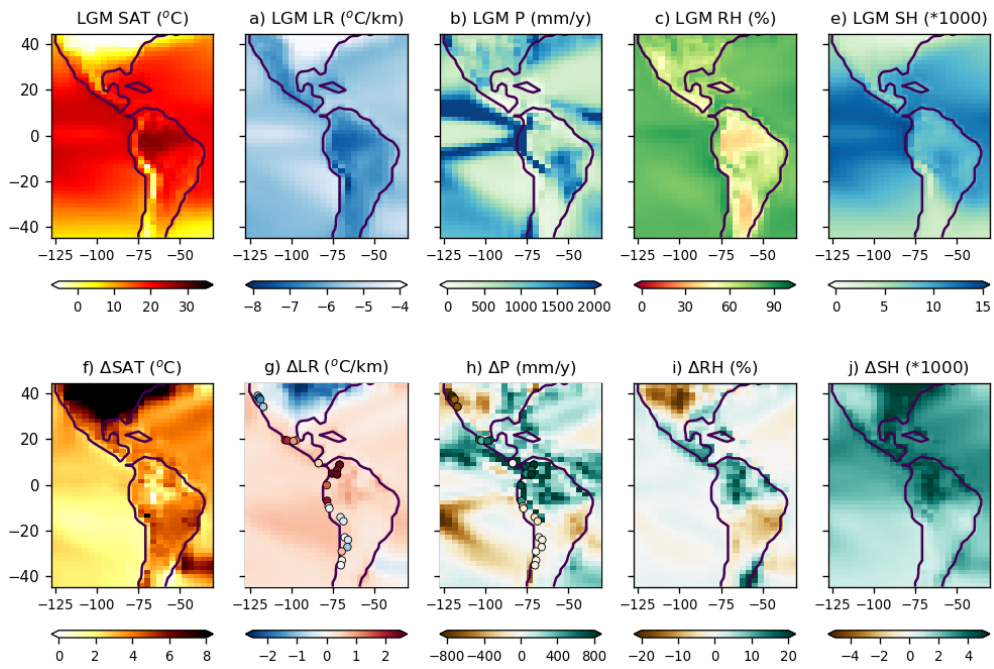
625 **Fig. 4 - A)** Low elevation vs high elevation post LGM warming. Low elevation T changes are calculated from  
 626 nearby SST, applying the continental correction factor (CFCE), while high elevation T changes are computed  
 627 from the glacier-derived  $0^{\circ}$  isotherm shift, using modern local lapse rates. B) Modern and LGM lapse rates C)  
 628  $\Delta LR_{(\text{modern-LGM})}$  for the 31 studied sites. Central tropics ( $20^{\circ}\text{N} - 9^{\circ}\text{S}$ ) present the highest value of  $\Delta LR_{(\text{modern-LGM})}$   
 629 and thus a steeper lapse rate during the LGM. Post-deglacial warming is thus amplified at high-altitude, between  
 630  $20^{\circ}\text{N} - 9^{\circ}\text{S}$ .

631



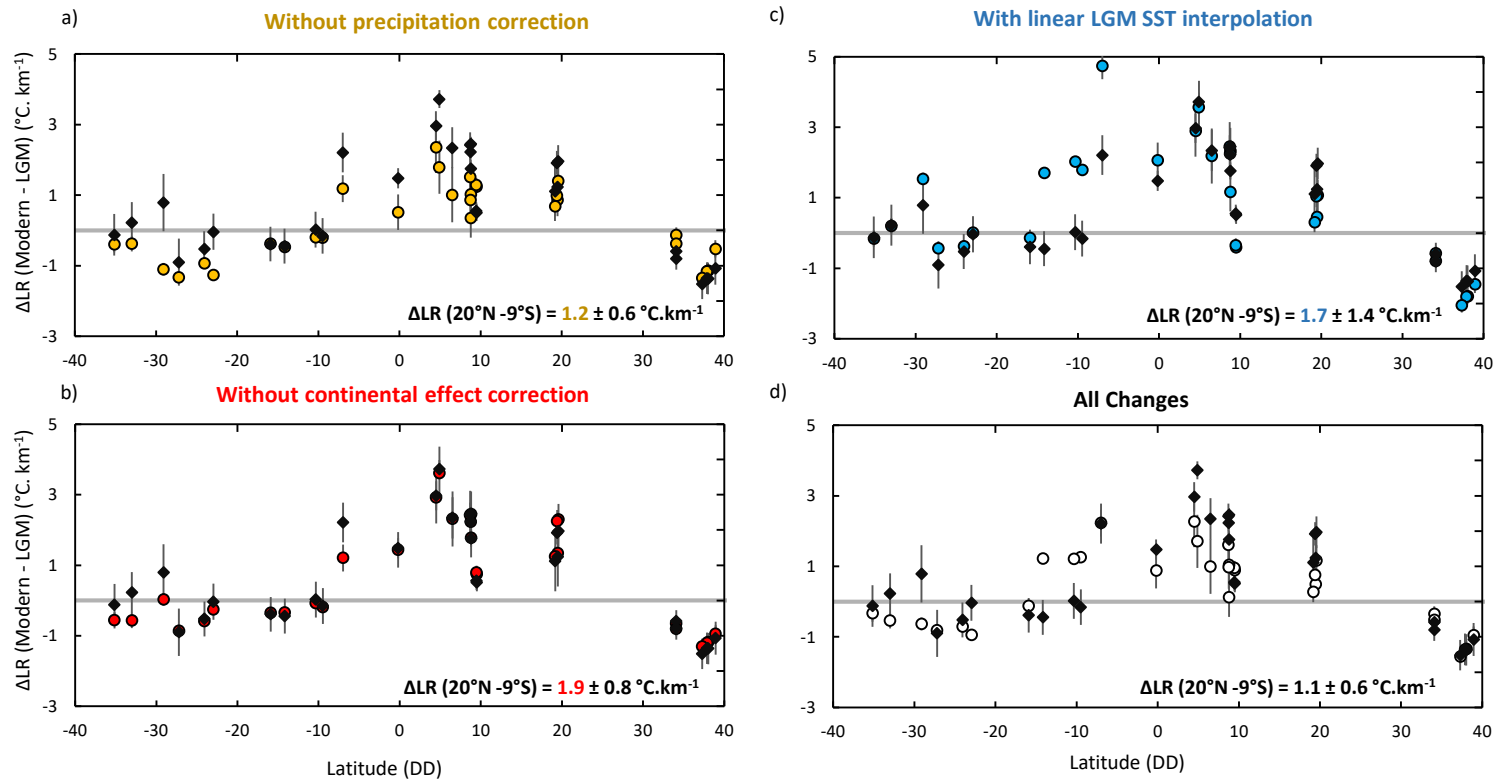
632  
633

634 **Fig. 5:** Annual precipitation (mm) plotted against lapse rates, for both modern (orange circles) and LGM (blue  
635 circles) lapse rates (Lower panel). Box plot showing the distribution of modern and LGM lapse rates (Upper  
636 panel).



637

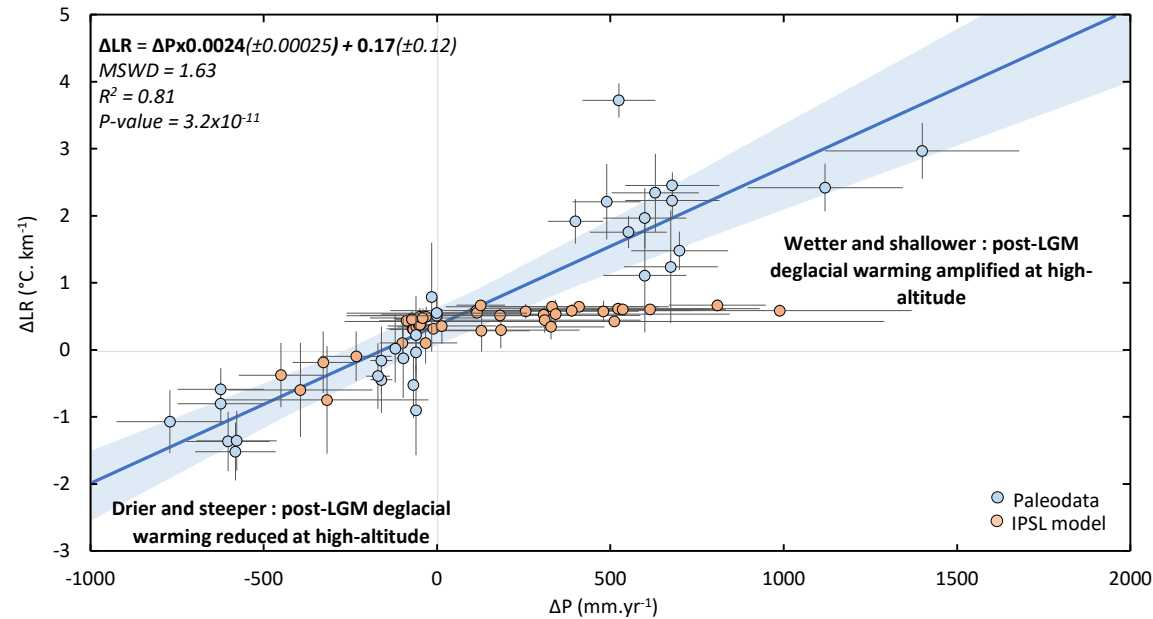
638 **Fig. 6:** IPSLCM5A2 coupled model results for the LGM climate (top row) and the PI – LGM anomaly (bottom  
 639 row). Surface air temperature (a: LGM, f: PI – LGM), lapse rate (b: LGM, g: PI – LGM), annual precipitation (c:  
 640 LGM, h: PI – LGM), relative humidity (d: LGM, i: PI – LGM), and specific humidity (e: LGM, j: PI – LGM). All  
 641 fields are annual means. Reconstructions compiled in this study for the lapse rate and precipitation are  
 642 superimposed on panels e and f, based on the same colour scale as for the maps.



643

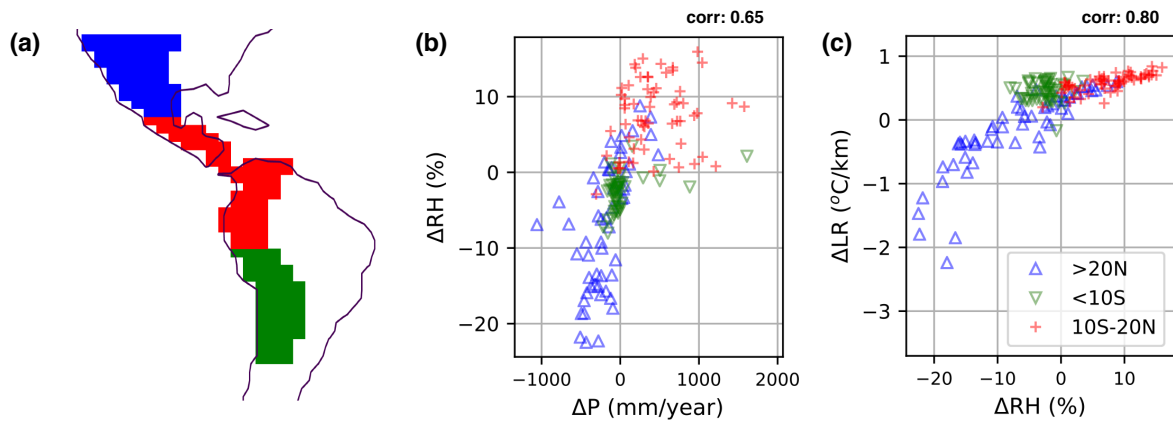
644 **Fig. 7:** Testing the model dependence of  $\Delta LR$  results. Dark diamonds are the computed  $\Delta LR$  of the study (see methods, Fig.5). Coloured dots show  $\Delta LR$  computed removing  
 645 iteratively each correction: a)  $\Delta LR$  computed without precipitation correction (yellow dots), b)  $\Delta LR$  computed without CFCE correction (red dots), c)  $\Delta LR$  computed assuming  
 646 that corresponding LGM SSTs are interpolated from the 2 nearest cores, without using the SST calibration relationship (blue dots). d)  $\Delta LR$  computed without performing any  
 647 of the 3 corrections (white dots). Note that  $\Delta LR$  between  $20^{\circ}\text{N}$  and  $9^{\circ}\text{S}$  is significantly superior to zero independently of the modelling choices used.

648



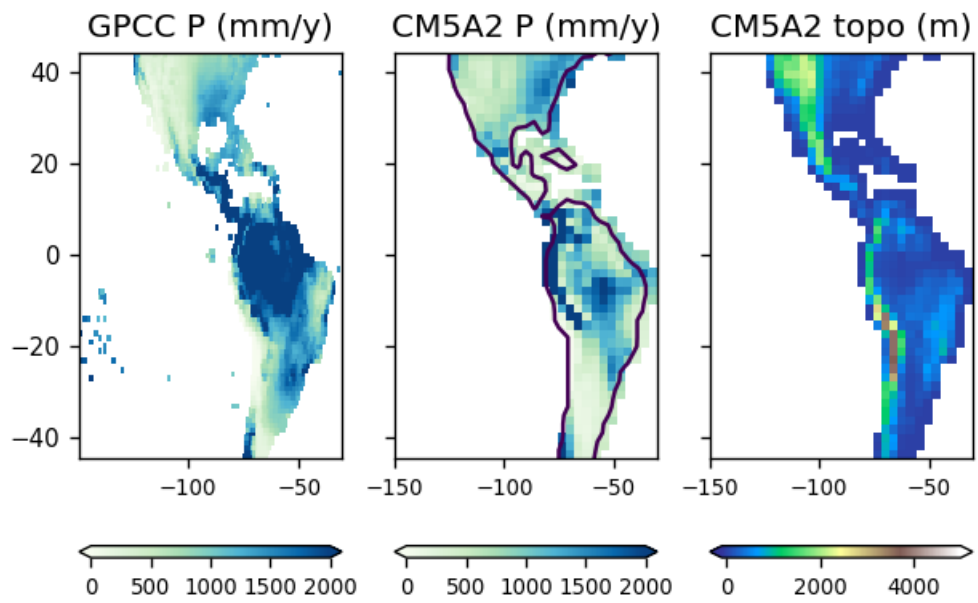
649

650 **Fig. 8:** Correlation between  $\Delta LR$  and  $\Delta P$ . (a) Data, blue dots: LGM precipitation has been calculated directly from modern precipitation and independent paleoprecipitation  
 651 proxy (See Methods). The 31 sites of calculation are shown as blues dots. Note that steeper and shallower modern LR are systemically associated with drier and wetter areas  
 652 than during LGM, respectively. IPSL model, orange dots: precipitation and lapse rate variations have been extracted at each data site location to perform the comparison.



653  
 654  
 655  
 656  
 657  
 658

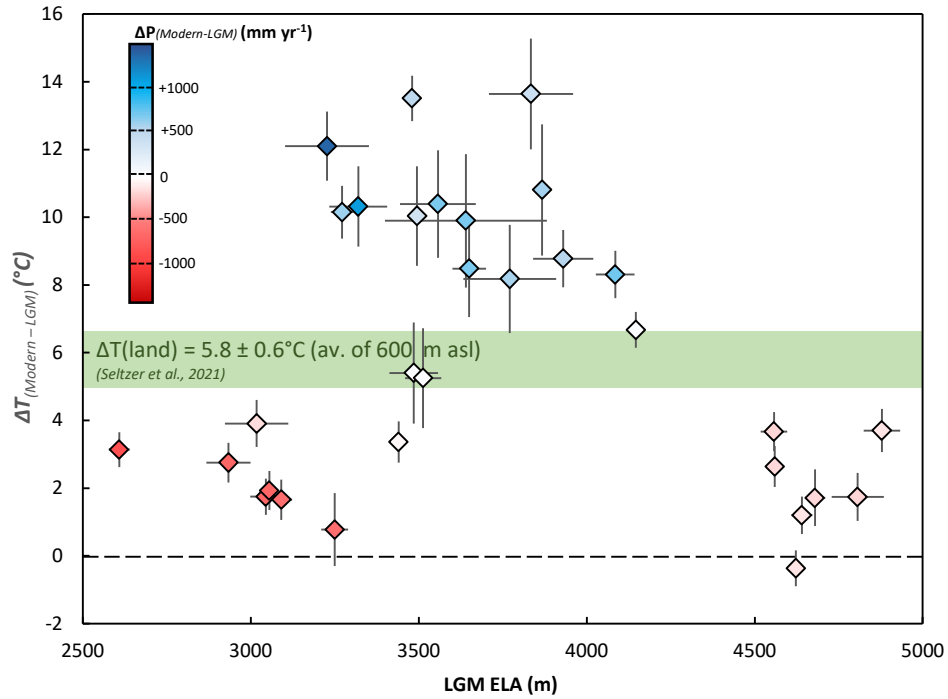
**Fig. 9:** Relationships between variables simulated by IPSLCM5A2 over and close to the American Cordillera, on the grid points highlighted on the map. The American Cordillera is separated into three main domains highlighted in green, red and blue (a), respectively.  $\Delta$  indicate PI - LGM anomalies. RH: relative humidity at first level, P: precipitation, LR : lapse rate.



659

660 **Fig. 10:** Comparison of observed (GPCC dataset,  
 661 [https://opendata.dwd.de/climate\\_environment/GPCC/html/gpcc\\_normals\\_v2022\\_doi\\_download.html](https://opendata.dwd.de/climate_environment/GPCC/html/gpcc_normals_v2022_doi_download.html)) and  
 662 modeled (GCM IPSLCM5A2) modern precipitation field in the American Cordillera

663



664

665 **Fig. 11:** Correlation between  $\Delta T_{(Modern-LGM)}$  and LGM ELA (m).  $\Delta T_{(Modern-LGM)}$  is computed from the ELA  
 666 depression value using the modern lapse rate value. Blue and red dots represent sites that were drier and wetter  
 667 during the LGM relative to present-day, respectively. LGM precipitation was calculated directly from modern  
 668 precipitation and independent paleoprecipitation proxies (see Methods). Note that the highest values of  $\Delta T$  are  
 669 higher than the land  $\Delta T$  from the study of Seltzer et al. (2021)(green shaded area).

670

671 **References**

- 672 Abe-Ouchi, A., Saito, F., Kageyama, M., Braconnot, P., Harrison, S.P., Lambeck, K., Otto-Bliesner, B.L.,  
673 Peltier, W.R., Tarasov, L., Peterschmitt, J.-Y., Takahashi, K., 2015. Ice-sheet configuration in  
674 the CMIP5/PMIP3 Last Glacial Maximum experiments. *Geosci. Model Dev.* 8, 3621–3637.  
675 <https://doi.org/10.5194/gmd-8-3621-2015>
- 676 Ammann, C., Jenny, B., Kammer, K., Messerli, B., 2001. Late Quaternary Glacier response to humidity  
677 changes in the arid Andes of Chile (18–29°S). *Palaeogeography, Palaeoclimatology,*  
678 *Palaeoecology* 172, 313–326. [https://doi.org/10.1016/S0031-0182\(01\)00306-6](https://doi.org/10.1016/S0031-0182(01)00306-6)
- 679 Annan, J.D., Hargreaves, J.C., Mauritsen, T., 2022. A new global surface temperature reconstruction  
680 for the Last Glacial Maximum. *Clim. Past* 18, 1883–1896. [https://doi.org/10.5194/cp-18-](https://doi.org/10.5194/cp-18-1883-2022)  
681 [1883-2022](https://doi.org/10.5194/cp-18-1883-2022)
- 682 Bartlein, P.J., Harrison, S.P., Brewer, S., Connor, S., Davis, B.A.S., Gajewski, K., Guiot, J., Harrison-  
683 Prentice, T.I., Henderson, A., Peyron, O., Prentice, I.C., Scholze, M., Seppä, H., Shuman, B.,  
684 Sugita, S., Thompson, R.S., Viau, A.E., Williams, J., Wu, H., 2011. Pollen-based continental  
685 climate reconstructions at 6 and 21 ka: a global synthesis. *Clim Dyn* 37, 775–802.  
686 <https://doi.org/10.1007/s00382-010-0904-1>
- 687 Benn, D.I., Lehmkuhl, F., 2000. Mass balance and equilibrium-line altitudes of glaciers in high-  
688 mountain environments. *Quaternary International* 65–66, 15–29.  
689 [https://doi.org/10.1016/S1040-6182\(99\)00034-8](https://doi.org/10.1016/S1040-6182(99)00034-8)
- 690 Bhattacharya, T., Tierney, J.E., Addison, J.A., Murray, J.W., 2018. Ice-sheet modulation of deglacial  
691 North American monsoon intensification. *Nature Geosci* 11, 848–852.  
692 <https://doi.org/10.1038/s41561-018-0220-7>
- 693 Blard, P.-H., Lavé, J., Pik, R., Wagnon, P., Bourlès, D., 2007a. Persistence of full glacial conditions in  
694 the central Pacific until 15,000 years ago. *Nature* 449, 591–594.  
695 <https://doi.org/10.1038/nature06142>
- 696 Blard, P.-H., Lavé, J., Pik, R., Wagnon, P., Bourlès, D., 2007b. Persistence of full glacial conditions in  
697 the central Pacific until 15,000 years ago. *Nature* 449, 591–594.  
698 <https://doi.org/10.1038/nature06142>
- 699 Blard, P.-H., Sylvestre, F., Tripathi, A.K., Claude, C., Causse, C., Coudrain, A., Condom, T., Seidel, J.-L.,  
700 Vimeux, F., Moreau, C., Dumoulin, J.-P., Lavé, J., 2011. Lake highstands on the Altiplano  
701 (Tropical Andes) contemporaneous with Heinrich 1 and the Younger Dryas: new insights from  
702  $^{14}\text{C}$ , U–Th dating and  $\delta^{18}\text{O}$  of carbonates. *Quaternary Science Reviews* 30, 3973–3989.  
703 <https://doi.org/10.1016/j.quascirev.2011.11.001>
- 704 Bova, S., Rosenthal, Y., Liu, Z., Godad, S.P., Yan, M., 2021. Seasonal origin of the thermal maxima at  
705 the Holocene and the last interglacial. *Nature* 589, 548–553.  
706 <https://doi.org/10.1038/s41586-020-03155-x>
- 707 Clark, P.U., Dyke, A.S., Shakun, J.D., Carlson, A.E., Clark, J., Wohlfarth, B., Mitrovica, J.X., Hostetler,  
708 S.W., McCabe, A.M., 2009. The Last Glacial Maximum. *Science* 325, 710–714.  
709 <https://doi.org/10.1126/science.1172873>
- 710 Cleator, S., Harrison, S., Nichols, N., Prentice, I.C., Roulstone, I., 2019. A new multi-variable  
711 benchmark for Last Glacial Maximum climate simulations.  
712 <https://doi.org/10.17864/1947.229>
- 713 Condom, T., Coudrain, A., Sicart, J.-E., Théry, S., 2007. Computation of the space and time evolution  
714 of equilibrium-line altitudes on Andean glaciers (10 degrees N-55 degrees S). *Global and*  
715 *Planetary Change*.
- 716 Denham, T., Haberle, S., 2008. Agricultural emergence and transformation in the Upper Wahgi valley,  
717 Papua New Guinea, during the Holocene: theory, method and practice. *The Holocene* 18,  
718 481–496. <https://doi.org/10.1177/0959683607087936>
- 719 Dutton, A., Carlson, A.E., Long, A.J., Milne, G.A., Clark, P.U., DeConto, R., Horton, B.P., Rahmstorf, S.,  
720 Raymo, M.E., 2015. Sea-level rise due to polar ice-sheet mass loss during past warm periods.  
721 *Science* 349, aaa4019. <https://doi.org/10.1126/science.aaa4019>

722 Fleming, K., Johnston, P., Zwartz, D., Yokoyama, Y., Lambeck, K., Chappell, J., 1998. Refining the  
723 eustatic sea-level curve since the Last Glacial Maximum using far- and intermediate-field  
724 sites. *Earth and Planetary Science Letters* 163, 327–342. [https://doi.org/10.1016/S0012-](https://doi.org/10.1016/S0012-821X(98)00198-8)  
725 [821X\(98\)00198-8](https://doi.org/10.1016/S0012-821X(98)00198-8)

726 Fox, A., Bloom, A., 1994. Snowline altitude and climate in the Peruvian Andes (5°-17° S) at present  
727 and during the Latest Pleistocene Glacial Maximum. *Journal of Geography* 103, 867–885.

728 Herbert, T.D., Schuffert, J.D., Andreasen, D., Heusser, L., Lyle, M., Mix, A., Ravelo, A.C., Stott, L.D.,  
729 Herguera, J.C., 2001. Collapse of the California Current During Glacial Maxima Linked to  
730 Climate Change on Land. *Science* 293, 71–76. <https://doi.org/10.1126/science.1059209>

731 Hope, G., 2009. Environmental change and fire in the Owen Stanley Ranges, Papua New Guinea.  
732 *Quaternary Science Reviews* 28, 2261–2276.  
733 <https://doi.org/10.1016/j.quascirev.2009.04.012>

734 Huang, B., Banzon, V.F., Freeman, E., Lawrimore, J., Liu, W., Peterson, T.C., Smith, T.M., Thorne, P.W.,  
735 Woodruff, S.D., Zhang, H.-M., 2015. Extended Reconstructed Sea Surface Temperature  
736 Version 4 (ERSST.v4). Part I: Upgrades and Intercomparisons. *Journal of Climate* 28, 911–930.  
737 <https://doi.org/10.1175/JCLI-D-14-00006.1>

738 Hugonnet, R., McNabb, R., Berthier, E., Menounos, B., Nuth, C., Girod, L., Farinotti, D., Huss, M.,  
739 Dussailant, I., Brun, F., Kääb, A., 2021. Accelerated global glacier mass loss in the early  
740 twenty-first century. *Nature* 592, 726–731. <https://doi.org/10.1038/s41586-021-03436-z>

741 Intergovernmental Panel on Climate Change (IPCC), 2022. *The Ocean and Cryosphere in a Changing*  
742 *Climate: Special Report of the Intergovernmental Panel on Climate Change*, 1st ed.  
743 Cambridge University Press. <https://doi.org/10.1017/9781009157964>

744 Kageyama, M., Albani, S., Braconnot, P., Harrison, S.P., Hopcroft, P.O., Ivanovic, R.F., Lambert, F.,  
745 Marti, O., Peltier, W.R., Peterschmitt, J.-Y., Roche, D.M., Tarasov, L., Zhang, Xu, Brady, E.C.,  
746 Haywood, A.M., LeGrande, A.N., Lunt, D.J., Mahowald, N.M., Mikolajewicz, U., Nisancioglu,  
747 K.H., Otto-Bliesner, B.L., Renssen, H., Tomas, R.A., Zhang, Q., Abe-Ouchi, A., Bartlein, P.J.,  
748 Cao, J., Li, Q., Lohmann, G., Ohgaito, R., Shi, X., Volodin, E., Yoshida, K., Zhang, Xiao, Zheng,  
749 W., 2017. The PMIP4 contribution to CMIP6 – Part 4: Scientific objectives and experimental  
750 design of the PMIP4-CMIP6 Last Glacial Maximum experiments and PMIP4 sensitivity  
751 experiments. *Geosci. Model Dev.* 10, 4035–4055. [https://doi.org/10.5194/gmd-10-4035-](https://doi.org/10.5194/gmd-10-4035-2017)  
752 [2017](https://doi.org/10.5194/gmd-10-4035-2017)

753 Kageyama, M., Harrison, S.P., Kapsch, M.-L., Lofverstrom, M., Lora, J.M., Mikolajewicz, U., Sherriff-  
754 Tadano, S., Vadsaria, T., Abe-Ouchi, A., Bouttes, N., Chandan, D., Gregoire, L.J., Ivanovic, R.F.,  
755 Izumi, K., LeGrande, A.N., Lhardy, F., Lohmann, G., Morozova, P.A., Ohgaito, R., Paul, A.,  
756 Peltier, W.R., Poulsen, C.J., Quiquet, A., Roche, D.M., Shi, X., Tierney, J.E., Valdes, P.J.,  
757 Volodin, E., Zhu, J., 2021. The PMIP4 Last Glacial Maximum experiments: preliminary results  
758 and comparison with the PMIP3 simulations. *Clim. Past* 17, 1065–1089.  
759 <https://doi.org/10.5194/cp-17-1065-2021>

760 Kaser, G., Großhauser, M., Marzeion, B., 2010. Contribution potential of glaciers to water availability  
761 in different climate regimes. *Proc. Natl. Acad. Sci. U.S.A.* 107, 20223–20227.  
762 <https://doi.org/10.1073/pnas.1008162107>

763 Kattel, D.B., Yao, T., Yang, K., Tian, L., Yang, G., Joswiak, D., 2013. Temperature lapse rate in complex  
764 mountain terrain on the southern slope of the central Himalayas. *Theor Appl Climatol* 113,  
765 671–682. <https://doi.org/10.1007/s00704-012-0816-6>

766 Keil, P., Schmidt, H., Stevens, B., Bao, J., 2021. Variations of Tropical Lapse Rates in Climate Models  
767 and their Implications for Upper Tropospheric Warming. *Journal of Climate* 1–50.  
768 <https://doi.org/10.1175/JCLI-D-21-0196.1>

769 Kraaijenbrink, P.D.A., Bierkens, M.F.P., Lutz, A.F., Immerzeel, W.W., 2017. Impact of a global  
770 temperature rise of 1.5 degrees Celsius on Asia’s glaciers. *Nature* 549, 257–260.  
771 <https://doi.org/10.1038/nature23878>

772 Kuhlemann, J., Rohling, E.J., Krumrei, I., Kubik, P., Ivy-Ochs, S., Kucera, M., 2008. Regional Synthesis  
773 of Mediterranean Atmospheric Circulation During the Last Glacial Maximum. *Science* 321,  
774 1338–1340. <https://doi.org/10.1126/science.1157638>

775 Lachniet, M.S., Asmerom, Y., Bernal, J.P., Polyak, V.J., Vazquez-Selem, L., 2013. Orbital pacing and  
776 ocean circulation-induced collapses of the Mesoamerican monsoon over the past 22,000 y.  
777 *Proc. Natl. Acad. Sci. U.S.A.* 110, 9255–9260. <https://doi.org/10.1073/pnas.1222804110>

778 Lachniet, M.S., Vazquez-Selem, L., 2005. Last Glacial Maximum equilibrium line altitudes in the  
779 circum-Caribbean (Mexico, Guatemala, Costa Rica, Colombia, and Venezuela). *Quaternary*  
780 *International* 138–139, 129–144. <https://doi.org/10.1016/j.quaint.2005.02.010>

781 Lal, D., 1991. Cosmic ray labeling of erosion surfaces: in situ nuclide production rates and erosion  
782 models. *Earth and Planetary Science Letters* 104, 424–439.

783 Lea, D.W., Kienast, M., De Garidel-Thoron, T., Kageyama, M., Paul, A., Bard, E., 2014. COMPARE 2013:  
784 Constraining tropical ocean cooling during the Last Glacial Maximum. *PAGES Mag* 22, 43–43.  
785 <https://doi.org/10.22498/pages.22.1.43>

786 Leduc, G., Garidel-Thoron, T. de, Kaiser, J., Bolton, C., Contoux, C., 2017. Databases for sea surface  
787 paleotemperature based on geochemical proxies from marine sediments: implications for  
788 model-data comparisons. *quaternaire* 201–216. <https://doi.org/10.4000/quaternaire.8034>

789 Leduc, G., Schneider, R., Kim, J.-H., Lohmann, G., 2010. Holocene and Eemian sea surface  
790 temperature trends as revealed by alkenone and Mg/Ca paleothermometry. *Quaternary*  
791 *Science Reviews* 29, 989–1004. <https://doi.org/10.1016/j.quascirev.2010.01.004>

792 Leduc, G., Vidal, L., Tachikawa, K., Rostek, F., Sonzogni, C., Beaufort, L., Bard, E., 2007. Moisture  
793 transport across Central America as a positive feedback on abrupt climatic changes. *Nature*  
794 445, 908–911. <https://doi.org/10.1038/nature05578>

795 Legrain, E., Blard, P.-H., Charreau, J., 2022. Glacial equilibrium line–based relationship for  
796 paleoclimate reconstructions (Sierra Nevada, USA). *Quat. res.* 109, 183–194.  
797 <https://doi.org/10.1017/qua.2022.10>

798 Lifton, N., Sato, T., Dunai, T.J., 2014. Scaling in situ cosmogenic nuclide production rates using  
799 analytical approximations to atmospheric cosmic-ray fluxes. *Earth and Planetary Science*  
800 *Letters* 386, 149–160. <https://doi.org/10.1016/j.epsl.2013.10.052>

801 Loomis, S.E., Russell, J.M., Verschuren, D., Morrill, C., De Cort, G., Sinnighe Damsté, J.S., Olago, D.,  
802 Eggermont, H., Street-Perrott, F.A., Kelly, M.A., 2017. The tropical lapse rate steepened  
803 during the Last Glacial Maximum. *Sci. Adv.* 3, e1600815.  
804 <https://doi.org/10.1126/sciadv.1600815>

805 Marrero, S.M., Phillips, F.M., Caffee, M.W., Gosse, J.C., 2016. CRONUS-Earth cosmogenic <sup>36</sup>Cl  
806 calibration. *Quaternary Geochronology* 31, 199–219.  
807 <https://doi.org/10.1016/j.quageo.2015.10.002>

808 Martin, L.C.P., Blard, P.-H., Balco, G., Lavé, J., Delunel, R., Lifton, N., Laurent, V., 2017. The CREp  
809 program and the ICE-D production rate calibration database: A fully parameterizable and  
810 updated online tool to compute cosmic-ray exposure ages. *Quaternary Geochronology* 38,  
811 25–49. <https://doi.org/10.1016/j.quageo.2016.11.006>

812 Martin, L.C.P., Blard, P.-H., Lavé, J., Braucher, R., Lupker, M., Condom, T., Charreau, J., Mariotti, V.,  
813 ASTER Team, Davy, E., 2015. In situ cosmogenic <sup>10</sup>Be production rate in the High Tropical  
814 Andes. *Quaternary Geochronology* 30, 54–68. <https://doi.org/10.1016/j.quageo.2015.06.012>

815 Martin, L.C.P., Blard, P.-H., Lavé, J., Condom, T., Prémaillon, M., Jomelli, V., Brunstein, D., Lupker, M.,  
816 Charreau, J., Mariotti, V., Tibari, B., ASTER Team, Davy, E., 2018. Lake Tauca highstand  
817 (Heinrich Stadial 1a) driven by a southward shift of the Bolivian High. *Sci. Adv.* 4, eaar2514.  
818 <https://doi.org/10.1126/sciadv.aar2514>

819 Martin, L.C.P., Blard, P.-H., Lavé, J., Jomelli, V., Charreau, J., Condom, T., Lupker, M., Arnold, M.,  
820 Aumaître, G., Boursières, D.L., Keddadouche, K., 2020. Antarctic-like temperature variations in  
821 the Tropical Andes recorded by glaciers and lakes during the last deglaciation. *Quaternary*  
822 *Science Reviews* 247, 106542. <https://doi.org/10.1016/j.quascirev.2020.106542>

823 McGee, D., 2020. Glacial–Interglacial Precipitation Changes. *Annu. Rev. Mar. Sci.* 12, 525–557.  
824 <https://doi.org/10.1146/annurev-marine-010419-010859>

825 Meier, M., Post, A., 1962. Recent variations in mass net budgets of glaciers in western North  
826 America. *International Association of Scientific Hydrology Publications* 58.

827 Mountain Research Initiative EDW Working Group, 2015. Elevation-dependent warming in mountain  
828 regions of the world. *Nature Clim Change* 5, 424–430. <https://doi.org/10.1038/nclimate2563>

829 Mountain Research Initiative EDW Working Group, Pepin, N., Bradley, R.S., Diaz, H.F., Baraer, M.,  
830 Caceres, E.B., Forsythe, N., Fowler, H., Greenwood, G., Hashmi, M.Z., Liu, X.D., Miller, J.R.,  
831 Ning, L., Ohmura, A., Palazzi, E., Rangwala, I., Schöner, W., Severskiy, I., Shahgedanova, M.,  
832 Wang, M.B., Williamson, S.N., Yang, D.Q., 2015. Elevation-dependent warming in mountain  
833 regions of the world. *Nature Climate Change* 5, 424.

834 Muscheler, R., Beer, J., Kubik, P.W., Synal, H.-A., 2005. Geomagnetic field intensity during the last  
835 60,000 years based on 10Be and 36Cl from the Summit ice cores and 14C. *Quaternary*  
836 *Science Reviews* 24, 1849–1860. <https://doi.org/10.1016/j.quascirev.2005.01.012>

837 Nishiizumi, K., Imamura, M., Caffee, M.W., Southon, J.R., Finkel, R.C., McAninch, J., 2007. Absolute  
838 calibration of 10Be AMS standards. *Nuclear Instruments and Methods in Physics Research*  
839 *Section B: Beam Interactions with Materials and Atoms* 258, 403–413.  
840 <https://doi.org/10.1016/j.nimb.2007.01.297>

841 Ohmura, A., 2012. Enhanced temperature variability in high-altitude climate change. *Theor Appl*  
842 *Climatol* 110, 499–508. <https://doi.org/10.1007/s00704-012-0687-x>

843 Ohmura, A., 1992. Climate at the equilibrium line of glaciers. *Journal of Glaciology* 38.

844 Palacios, D., Stokes, C.R., Phillips, F.M., Clague, J.J., Alcalá-Reygosa, J., Andrés, N., Angel, I., Blard, P.-  
845 H., Briner, J.P., Hall, B.L., Dahms, D., Hein, A.S., Jomelli, V., Mark, B.G., Martini, M.A., Moreno,  
846 P., Riedel, J., Sagredo, E., Stansell, N.D., Vázquez-Selem, L., Vuille, M., Ward, D.J., 2020. The  
847 deglaciation of the Americas during the Last Glacial Termination. *Earth-Science Reviews* 203,  
848 103113. <https://doi.org/10.1016/j.earscirev.2020.103113>

849 Pandey, G.R., Cayan, D.R., Georgakakos, K.P., 1999. Precipitation structure in the Sierra Nevada of  
850 California during winter. *J. Geophys. Res.* 104, 12019–12030.  
851 <https://doi.org/10.1029/1999JD900103>

852 Pritchard, H.D., 2019. Asia’s shrinking glaciers protect large populations from drought stress. *Nature*  
853 569, 649–654. <https://doi.org/10.1038/s41586-019-1240-1>

854 Qixiang, W., Wang, M., Fan, X., 2018. Seasonal patterns of warming amplification of high-elevation  
855 stations across the globe. *Int J Climatol* 38, 3466–3473. <https://doi.org/10.1002/joc.5509>

856 Rabatel, A., Francou, B., Soruco, A., Gomez, J., Cáceres, B., Ceballos, J.L., Basantes, R., Vuille, M.,  
857 Sicart, J.-E., Huggel, C., Scheel, M., Lejeune, Y., Arnaud, Y., Collet, M., Condom, T., Consoli, G.,  
858 Favier, V., Jomelli, V., Galarraga, R., Ginot, P., Maisincho, L., Mendoza, J., Ménégoz, M.,  
859 Ramirez, E., Ribstein, P., Suarez, W., Villacis, M., Wagnon, P., 2013. Current state of glaciers  
860 in the tropical Andes: a multi-century perspective on glacier evolution and climate change.  
861 *The Cryosphere* 7, 81–102. <https://doi.org/10.5194/tc-7-81-2013>

862 Schimmelpfennig, I., Benedetti, L., Finkel, R., Pik, R., Blard, P.-H., Bournès, D., Burnard, P., Williams, A.,  
863 2009. Sources of in-situ 36Cl in basaltic rocks. Implications for calibration of production rates.  
864 *Quaternary Geochronology* 4, 441–461. <https://doi.org/10.1016/j.quageo.2009.06.003>

865 Seltzer, A.M., Blard, P.-H., Sherwood, S.C., Kageyama, M., 2023a. Terrestrial amplification of past,  
866 present, and future climate change. *Sci. Adv.* 9, eadf8119.  
867 <https://doi.org/10.1126/sciadv.adf8119>

868 Seltzer, A.M., Blard, P.-H., Sherwood, S.C., Kageyama, M., 2023b. Terrestrial amplification of past,  
869 present, and future climate change. *Sci. Adv.* 9, eadf8119.  
870 <https://doi.org/10.1126/sciadv.adf8119>

871 Seltzer, A.M., Ng, J., Aeschbach, W., Kipfer, R., Kulongoski, J.T., Severinghaus, J.P., Stute, M., 2021.  
872 Widespread six degrees Celsius cooling on land during the Last Glacial Maximum. *Nature* 593,  
873 228–232. <https://doi.org/10.1038/s41586-021-03467-6>

874 Sepulchre, P., Caubel, A., Ladant, J.-B., Bopp, L., Boucher, O., Braconnot, P., Brockmann, P., Cozic, A.,  
875 Donnadieu, Y., Dufresne, J.-L., Estella-Perez, V., Ethé, C., Fluteau, F., Foujols, M.-A.,  
876 Gastineau, G., Ghattas, J., Hauglustaine, D., Hourdin, F., Kageyama, M., Khodri, M., Marti, O.,  
877 Meurdesoif, Y., Mignot, J., Sarr, A.-C., Servonnat, J., Swingedouw, D., Szopa, S., Tardif, D.,  
878 2020. IPSL-CM5A2 – an Earth system model designed for multi-millennial climate  
879 simulations. *Geosci. Model Dev.* 13, 3011–3053. <https://doi.org/10.5194/gmd-13-3011-2020>  
880 Slater, D.A., Felikson, D., Straneo, F., Goelzer, H., Little, C.M., Morlighem, M., Fettweis, X., Nowicki, S.,  
881 2020. Twenty-first century ocean forcing of the Greenland ice sheet for modelling of sea level  
882 contribution. *The Cryosphere* 14, 985–1008. <https://doi.org/10.5194/tc-14-985-2020>  
883 Smith, D.M., Screen, J.A., Deser, C., Cohen, J., Fyfe, J.C., García-Serrano, J., Jung, T., Kattsov, V., Matei,  
884 D., Msadek, R., Peings, Y., Sigmond, M., Ukita, J., Yoon, J.-H., Zhang, X., 2019. The Polar  
885 Amplification Model Intercomparison Project (PAMIP) contribution to CMIP6: investigating  
886 the causes and consequences of polar amplification. *Geosci. Model Dev.* 12, 1139–1164.  
887 <https://doi.org/10.5194/gmd-12-1139-2019>  
888 Smith, T.M., Reynolds, R.W., 2003. Extended Reconstruction of Global Sea Surface Temperatures  
889 Based on COADS Data (1854–1997). *JOURNAL OF CLIMATE* 16.  
890 Stansell, N.D., Polissar, P.J., Abbott, M.B., 2007. Last glacial maximum equilibrium-line altitude and  
891 paleo-temperature reconstructions for the Cordillera de Mérida, Venezuelan Andes. *Quat.*  
892 *res.* 67, 115–127. <https://doi.org/10.1016/j.yqres.2006.07.005>  
893 Stone and Carlson, P., John, 1979. Atmospheric Lapse Rate Regimes and Their Parametrization.  
894 *Journal of the atmospheric sciences* 36, 415–423.  
895 Stute, M., Forster, M., Frischkorn, H., Serejo, A., Clark, J.F., Schlosser, P., Broecker, W.S., Bonani, G.,  
896 1995. Cooling of Tropical Brazil (5°C) During the Last Glacial Maximum. *Science* 269, 379–383.  
897 <https://doi.org/10.1126/science.269.5222.379>  
898 Thompson, L.G., Mosley-Thompson, E., Davis, M.E., Brecher, H.H., 2011. Tropical glaciers, recorders  
899 and indicators of climate change, are disappearing globally. *Ann. Glaciol.* 52, 23–34.  
900 <https://doi.org/10.3189/172756411799096231>  
901 Tierney, J.E., Zhu, J., King, J., Malevich, S.B., Hakim, G.J., Poulsen, C.J., 2020. Glacial cooling and  
902 climate sensitivity revisited. *Nature* 584, 569–573.  
903 Tripathi, A.K., Sahany, S., Pittman, D., Eagle, R.A., Neelin, J.D., Mitchell, J.L., Beaufort, L., 2014a.  
904 Modern and glacial tropical snowlines controlled by sea surface temperature and  
905 atmospheric mixing. *Nature Geosci* 7, 205–209. <https://doi.org/10.1038/ngeo2082>  
906 Tripathi, A.K., Sahany, S., Pittman, D., Eagle, R.A., Neelin, J.D., Mitchell, J.L., Beaufort, L., 2014b.  
907 Modern and glacial tropical snowlines controlled by sea surface temperature and  
908 atmospheric mixing. *Nature Geoscience* 7, DOI: 10.1038/NGeo2082.  
909 Wang, Q., Fan, X., Wang, M., 2016. Evidence of high-elevation amplification versus Arctic  
910 amplification. *Sci Rep* 6, 19219. <https://doi.org/10.1038/srep19219>  
911 Wang, Q., Fan, X., Wang, M., 2014. Recent warming amplification over high elevation regions across  
912 the globe. *Clim Dyn* 43, 87–101. <https://doi.org/10.1007/s00382-013-1889-3>  
913 Woods, A., Rodbell, D.T., Abbott, M.B., Hatfield, R.G., Chen, C.Y., Lehmann, S.B., McGee, D.,  
914 Weidhaas, N.C., Tapia, P.M., Valero-Garcés, B.L., Bush, M.B., Stoner, J.S., 2020. Andean  
915 drought and glacial retreat tied to Greenland warming during the last glacial period. *Nat*  
916 *Commun* 11, 5135. <https://doi.org/10.1038/s41467-020-19000-8>  
917 Zekollari, H., Huss, M., Farinotti, D., 2019. Modelling the future evolution of glaciers in the European  
918 Alps under the EURO-CORDEX RCM ensemble. *The Cryosphere* 13, 1125–1146.  
919 <https://doi.org/10.5194/tc-13-1125-2019>  
920 Zeng, Z., Wang, D., Yang, L., Wu, J., Ziegler, A.D., Liu, M., Ciais, P., Searchinger, T.D., Yang, Z.-L., Chen,  
921 D., Chen, A., Li, L.Z.X., Piao, S., Taylor, D., Cai, X., Pan, M., Peng, L., Lin, P., Gower, D., Feng, Y.,  
922 Zheng, C., Guan, K., Lian, X., Wang, T., Wang, L., Jeong, S.-J., Wei, Z., Sheffield, J., Caylor, K.,  
923 Wood, E.F., 2021. Deforestation-induced warming over tropical mountain regions regulated  
924 by elevation. *Nat. Geosci.* 14, 23–29. <https://doi.org/10.1038/s41561-020-00666-0>  
925